Received: 4 May 2023 | Revised: 21 August 2023 | Accepted: 31 August 2023

DOI: 10.1002/asna.20230075

Astronomische Nachrichten

ORIGINAL ARTICLE

The sulfur species in hot rocky exoplanet atmospheres

L. J. Janssen[1,2,3] | P. Woitke[4] | O. Herbort[5] | M. Min[6] | K. L. Chubb[3,7] | Ch. Helling[5,8] | L. Carone[4]

[1]Leiden Observatory, Leiden, The Netherlands

[2]Anton Pannekoek Institute for Astronomy, Amsterdam, The Netherlands

[3]Centre for Exoplanet Science, University of St Andrews, St. Andrews, UK

[4]Institut für Weltraumforschung, Österreichische Akademie der Wissenschaften, Graz, Austria

[5]Department of Astrophysics, University of Vienna, Wien, Austria

[6]SRON Netherlands Institute for Space Research, Utrecht, The Netherlands

[7]SUPA, School of Physics & Astronomy, University of St Andrews, St Andrews, UK

[8]Fakultät für Mathematik, Physik und Geodäsie, TU Graz, Graz, Austria

Correspondence
L. J. Janssen, Leiden Observatory, Niels Bohrweg 2, 2333 CA Leiden, The Netherlands.
Email: ljanssen@strw.leidenuniv.nl

Funding information
European Union, Grant/Award Number: 86047; STFC, Grant/Award Number: ST/V000861/1; European Union, Grant/Award Number: 101088557

Abstract

The first JWST observations of hot Jupiters showed an unexpected detection of SO_2 in their hydrogen-rich atmospheres. We investigate how much sulfur can be expected in the atmospheres of rocky exoplanets and which sulfur molecules can be expected to be most abundant and detectable by transmission spectroscopy. We run thermochemical equilibrium models at the crust–atmosphere interface, considering surface temperatures 500–5000 K, surface pressures 1–100 bar, and various sets of element abundances based on common rock compositions. Between 1000 and 2000 K, we find gaseous sulfur concentrations of up to 25% above the rock in our models. SO_2, SO, H_2S, and S_2 are by far the most abundant sulfur molecules. SO_2 shows potentially detectable features in transmission spectra at about 4 μm, between 7 and 8 μm, and beyond 15 μm. In contrast, the sometimes abundant H_2S molecule is difficult to detect in these spectra, which are mostly dominated by H_2O and CO_2. Although the molecule PS only occurs with concentrations < 300 ppm, it can cause a strong absorption feature between 0.3 and 0.65 μm in some of our models for high surface pressures. The detection of sulfur molecules would enable a better characterization of the planetary surface.

KEYWORDS

astrochemistry, planets and satellites: atmospheres, planets and satellites: terrestrial, techniques: spectroscopic, methods:numerical

1 | INTRODUCTION

In our Solar System, sulfur is the fifth most abundant volatile element Asplund et al. (2009), Gao et al. (2017), Asplund et al. (2021), with a sulfur/hydrogen ratio of $[S/H] = 10^{-4.85}$ (Lodders 2019). This is small compared with carbon $[C/H] = 10^{-3.53}$, nitrogen $[N/H] = 10^{-4.15}$, and oxygen $[O/H] = 10^{-3.29}$. It is therefore remarkable that the sulfur carrying species SO_2 was among the first new molecules discovered by the James Webb Space Telescope (JWST) in an exoplanet atmosphere. Sulfur dioxide SO_2 was observed in the gas giant WASP 39 b jointly with H_2O, CO_2, CO, and Na I (Rustamkulov et al. 2023). Tsai et al. (2023) suggest that the observed SO_2 is photochemically produced from H_2S, which actually is the main sulfur carrier in this atmosphere, but remained undetected. Their

model requires a large metallicity of 10× solar. Carone et al. (2023) argue that sulfur may be overabundant in the inner atmosphere in WASP 39 b compared with Mg, Si, and Fe, making it a candidate for tracing planet formation. Crossfield (2023) elaborates this idea by considering gas-phase kinetics for C/N/O/H/S species without the feedback of condensation processes. Earlier studies by Zahnle et al. (2016) for 51 Eri b did not predict large amounts of SO_2, but these authors used low metallicities and low irradiations in their exoplanet models.

The element sulfur plays a key role in the atmospheric chemistry of Venus (Krasnopolsky 2012; Rimmer et al. 2021), Jupiter Visscher et al. 2006, and its moon Io (Zolotov & Fegley 1999), Spencer et al. (2000), Moses et al. (2002), Lellouch et al. (2007). Mars does not show any traces of sulfur in its atmospheric spectrum (Encrenaz et al. 2011). Several sulfur-bearing species have been observed in the coma of comets such as 67P/Churyumov–Gerasimenko (Calmonte et al. 2016).

Venus is known to contain about 150 ppm SO_2 in its CO_2-rich atmosphere at $\sim$ 90 bar, with $[S/H] \approx 2$, and H_2SO_4 cloud particles at $\sim$ 1 bar (Rimmer et al. 2021, see references of previous modelling work on the Venusian atmosphere in this article).

Visscher et al. (2006) modeled Jupiter's atmospheric conditions and found sulfur being predominantly present in the form of H_2S. Photolysis of H_2S could be a step in the chemical reaction chain toward sulfur hazes (Gao et al. 2017). These aerosols are expected to have a smoothing effect on infrared transit spectra of exoplanets (e.g. Dymont et al. 2021; Gao et al. 2021). Both laboratory and space research studies have shown that sulfur can stimulate haze formation. He et al. (2020) conducted laboratory experiments and confirm this for warm, CO_2-rich atmospheres. Haze particles can form, e.g. from S_8-molecules (Zahnle et al. 2016), and act as a catalyzer, triggering reactions of species such as NH_3 or CH_4, which can change the optical appearance of the respective spectral features.

During the SL-9 impact on Jupiter, large amounts of CS, CS_2, and OCS were detected in the impact region, but SO and SO_2 were not (Zahnle & Mac Low 1994). The authors argue that these detections are an indicator for a local carbon to oxygen ratio of $C/O > 1$, in which case sulfur forms CS, CS_2, and OCS, whereas in the case $C/O < 1$, sulfur would form SO and SO_2. In protoplanetary disks, high CS and low SO and SO_2 abundances have been suggested as indicators for a high C/O ratio (Le Gal et al. 2021).

The simplest and most straightforward approach to model the near-crust composition of exoplanet atmospheres is to assume thermochemical equilibrium at the interface between planet crust and atmosphere. While the computation of gas phase equilibrium concentrations has been long established, for example, by Tsuji (1973), Gail et al. (1984), Allard & Hauschildt (1995), Woitke & Helling (2004), it is the inclusion of solid and liquid species in phase equilibrium that allows us to discuss the composition of gases above silicate materials, for example Lodders & Fegley (2002), Hashimoto et al. (2007), Schaefer et al. (2012), Ito et al. (2015), Woitke et al. (2018), Wood et al. (2019), Fegley et al. (2020), Herbort et al. (2020), and Fegley, Lodders, and Jacobson (2023). In particular, Fegley et al. (2016) have studied the solubility of rock in steam atmospheres. Schaefer et al. (2012) and Herbort et al. (2020) have calculated the chemical composition of the near-crust gas above common rock materials as function of surface temperature and pressure, showing a large variety of results for different element mixtures. Recently, Timmermann et al. (2023) have developed an open-source python code for equilibrium condensation, and compared their results with those of GGCHEM (Woitke et al. 2018). Fegley et al. (2023b) have published an extensive study of 69 elements in thermochemical equilibrium, using dry and wet Bulk Silicate Earth (BSE) abundances. Considering temperature 1000–4500 K, they conclude that the silicate vapor behaves ideally at least up to 100 bars, and discuss the effects of treating the silicate melt as a nonideal solution.

The validity of such an equilibrium approach can be questioned. For example, Hobbs et al. (2021) used a combination of LEVI, a photo-chemical kinetics code, and FastChem (Stock et al. 2018), a thermochemical equilibrium solver to study the sulfur chemistry on hot Jupiters. The authors compared their modeling results with a model proposed by Wang et al. (2017) and showed that thermochemistry dominates in most parts—except for the uppermost layers—for the example of a $T_{eq} = 2000$ K atmosphere with solar metallicity. Rimmer et al. (2021) showed that thermochemical equilibrium can simultaneously explain the crust composition and near-crust gas composition of Venus.

Arriving at similar conclusions, Shulyak et al. (2020) modeled hot Jupiter atmospheres around A0, F0, G2, and K0 stars for temperatures around 2000 K. They demonstrated that disequilibrium processes such as vertical mixing and stellar XUV radiation do not change the spectral results much at these temperatures. However, for lower temperatures around 1000 K the picture changes. Shulyak et al. predicted that the molecular mixing ratios in such UV-dominated atmospheres are strongly affected by disequilibrium processes, and possibly detectable with the James Webb Space Telescope (JWST).

The main JWST targets will be hot Jupiters and close in rocky exoplanets with equilibrium temperatures between about 900 and 2200 K around stars of types FKGM (Kolecki & Wang 2021; Stevenson et al. 2016). For these

objects, an application of thermochemical models can at least provide a good starting point for the composition of their atmospheres. To classify the chemistry in these atmospheres, it is an important question whether sulfur molecules might be detectable.

The observable concentrations of sulfur molecules in the atmospheres of rocky exoplanets are linked to the sulfur abundance (and those of the other elements) in the crust, which is ultimately set by planet formation and evolution. These conditions include, among other factors, the temperature conditions and availability of elements during planet formation and the proximity to the star, for example Andrews et al. (2018), Kama et al. (2019), Khorshid et al. (2021), Cevallos Soto et al. (2022), Speedie et al. (2022) Depending on the element abundances present in the planet's crust and surface, the atmospheric conditions can vary from oxidizing to reducing (Ortenzi et al. 2020), and evolve with time. Observational data for the atmospheres of rocky planets are still very sparse even if utilizing JWST (Greene et al. 2023; Wordsworth & Kreidberg 2021).

In Section 2, we run thermochemical equilibrium models to predict the abundances of sulfur molecules in the near-crust atmosphere, and determine which are the most abundant sulfur molecules to be expected in the atmosphere of hot rocky planets. In Section 3, we run simple radiative transfer models based on hydrostatic model atmospheres with constant temperature and chemical composition to find out which sulfur molecules might be detectable. We use ARCiS (Min et al. 2020) to generate transmission spectra, and then simulate JWST/NIRSpec and JWST/MIRI observations in Section 4, to discuss which spectral fingerprints of sulfur molecules might be detectable. We conclude and discuss our findings in Section 5.

2 | PHASE EQUILIBRIUM MODELS

2.1 | Modeling approach

We use the principle of minimization of Gibbs free energy to determine both the chemical composition of the gas and the material composition of the crust at the surface of a rocky planet. We use the Fortran code GGCHEM (Woitke et al. 2018) in this work. Similar phase equilibrium models have been developed, e.g., by Lodders & Fegley (2002), Schaefer et al. (2012), Ito et al. (2015), Fegley et al. (2016), Wood et al. (2019), and Timmermann et al. (2023). Our modeling approach is visualized by fig. 1 in Herbort et al. (2020). A given set of total element abundances is considered in chemical and phase equilibrium at pressure p and temperature T, assuming an equilibrium between outgassing and deposition. The code determines which condensates are stable, how much of these condensates are deposited, and calculates the composition of the remaining gas phase in contact with them. The results include the chemical concentrations of all considered sulfur molecules. The resulting fractions of the condensed species are interpreted as the surface mineral composition of the rocky exoplanet. The GGCHEM model assumes a mixture of ideal gases, so we use partial pressures instead of the more general concept of fugacities.

Our model includes 18 elements (H, C, N, O, F, Na, Mg, Al, Si, P, S, Cl, K, Ca, Ti, Cr, Mn, and Fe). According to this selection of elements, GGCHEM finds 471 molecules (71 of them contain sulfur) and 208 liquid and solid condensates in its database. We do not include silicic acid as a gaseous species (as proposed by Fegley et al. 2016)). Concerning the assumed total element abundances prior to condensation, we consider the following 10 datasets as described in Herbort et al. (2020) and Herbort et al. (2022): Bulk Silicate Earth (BSE), Continental Crust (CC), CI chondrite (CI), Mid Oceanic Ridge Basalt (MORB), Archean, present Earth (see Appendix A in Herbort et al. 2022), and solar abundances. We also consider Polluted White Dwarf (PWD) compositions. The spectroscopic measurements of PWDs (e.g., (e.g. Bonsor et al. 2020)) do not allow for certain key element abundances to be determined, in particular hydrogen, but also nitrogen, fluorine, and chlorine, to mention a few. We therefore completed one basic PWD dataset of element mass fractions (Melis & Dufour 2016) with the mass fractions of the missing elements from either BSE, CC, or CI, see tab. 2 in Herbort et al. (2022) for more details. For example, the notation PWD-BSE means that we consider base PWD abundances, completed by BSE abundances.

2.2 | Resulting gas compositions

Similar to Hashimoto et al. (2007), Schaefer et al. (2012), and Fegley et al. (2016), we studied the gas phase composition above rocks in models for $p = 1$ bar and 100 bar. Table B1 lists our results for the 10 different sets of total element abundances in form of the main molecules and condensates that occur at different temperatures between 100 K and 5000 K for a constant surface pressure of $p = 100$ bar. This pressure is similar to Venus' surface pressure. We also list the sulfur concentrations that result to remain in the gas phase, i.e., in the atmosphere.

Figure 1 plots the same results as function of temperature. According to these results, rocky exoplanet atmospheres can contain up to 25% of gaseous sulfur. This maximum value is found at 3000 K and 100 bar in the

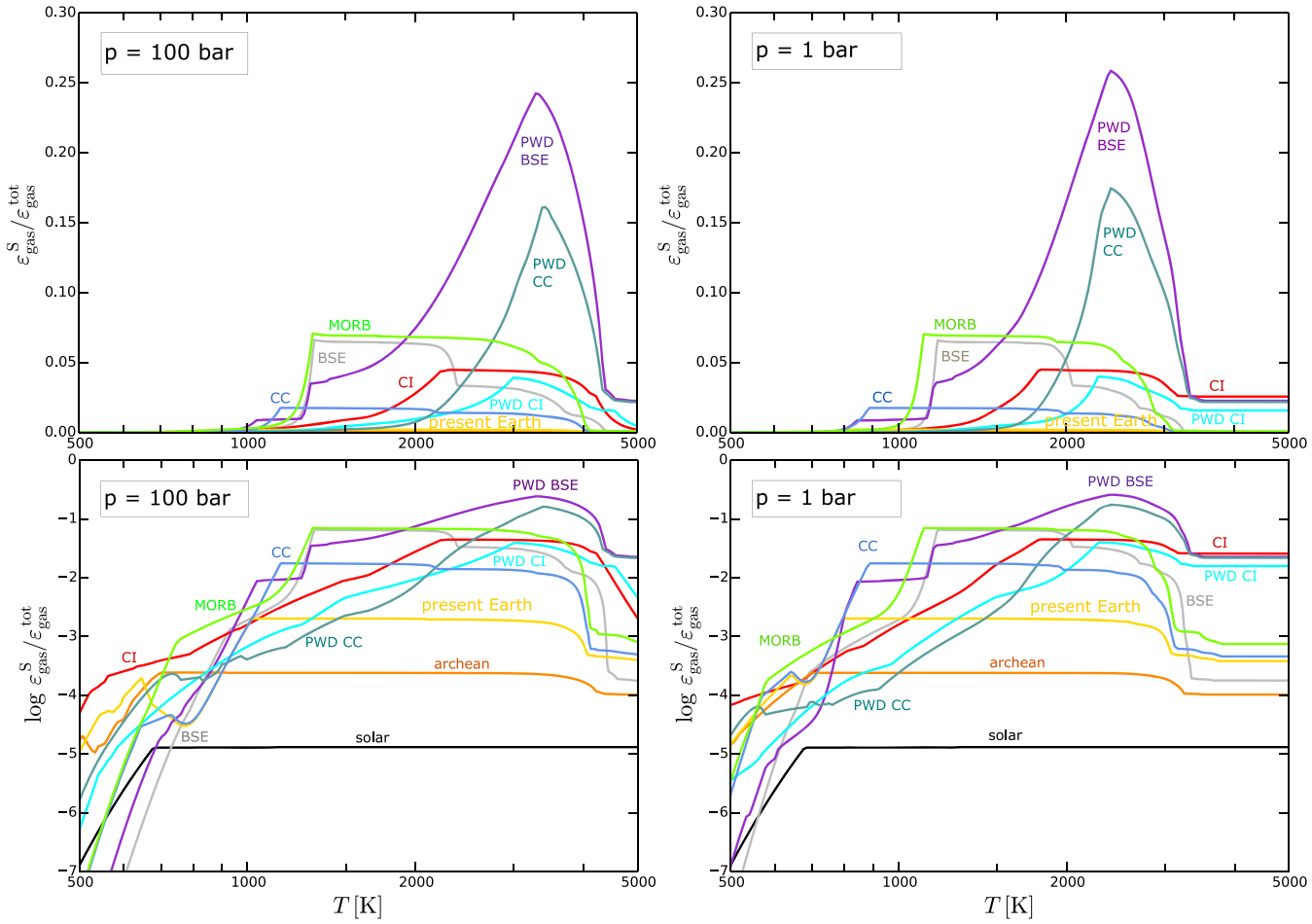

FIGURE 1 Sulfur abundances in the gas over rocky surfaces of different materials (labeled) as function of temperature. ϵ^{S}_{gas} is the element abundance of S in the gas phase and ϵ^{tot}_{gas} the sum of all element abundances in the gas phase. Results are shown on a linear axis on the top, and on a logarithmic axis at the bottom. The left and right figures show the results for 100 and 1 bar, respectively. The material labels are explained in Section 2.1.

PWD-BSE model. This gaseous elemental sulfur concentration is significantly higher, for example, than in our model with Earth-like element abundances, where it only reaches a maximum of about 1.7% at about 1000 K.

Both Tables B1 and B2 show that all models (except for the hydrogen-rich CI chondrite model) are featured by an N_2-rich atmosphere at the lowest temperatures. As the hydrogen content in CI chondrite atmospheres is high, NH_3 replaces N_2 at these temperatures. Ammonia is further discussed in Hashimoto et al. (2007) and Schaefer & Fegley (2007).

Similar to gas giants, such compositions would be classified as an A-type atmosphere following the scheme of Woitke et al. (2020) based on H, C, N, O element abundances. We have extended this classification to include sulfur in Appendix A. It provides a very helpful scheme to understand the very complex sulfur chemistry and the condensations that can occur therein (Table A2). The sulfur chemistry is not only characterized by the redox state (see y-axis in Figure A1), but we have a two-dimensional problem, where a suitable second axis is found to be a relative carbon content in the gas (see x-axis in Figure A1). The molecule CO_2, which is predicted to be abundant in type B and type C atmospheres, cannot form in A-type atmospheres. And the molecule CH_4, which is found to be abundant in type A and C atmospheres, cannot form in B-type atmospheres.

Figure 2 shows the results of one of our equilibrium condensation models in more detail. We selected the BSE model at $p = 1$ bar for this plot, see Table B2 for details. The relative sulfur abundance in the gas phase peaks around 1000–2000 K (green line, labeled S), reaching a maximum value of about 6.5%. At these temperatures, sulfur becomes the third most abundant element in the gas phase after hydrogen and oxygen, more abundant than carbon and nitrogen. The family names of condensates used in the upper part of Figure 2 are explained in the Appendix in Table B4.

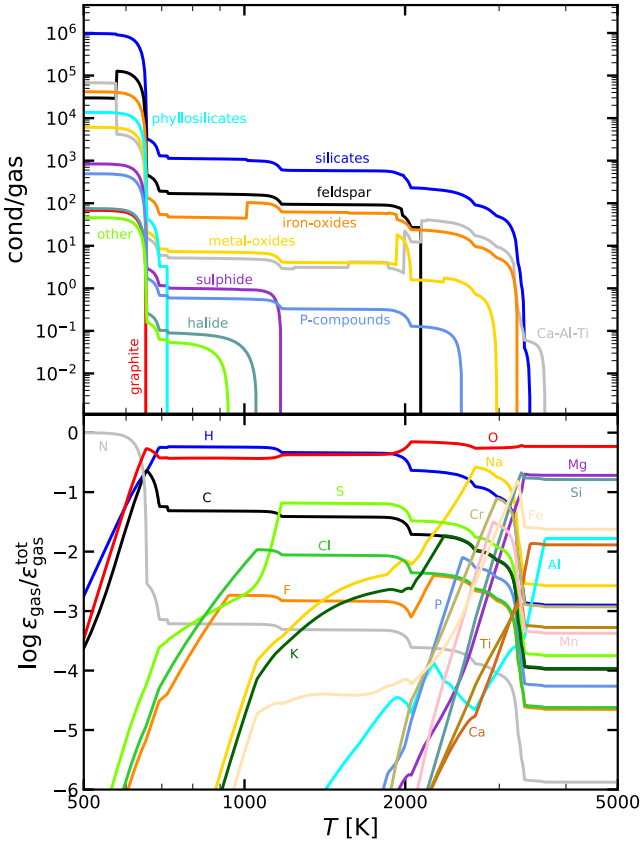

FIGURE 2 Equilibrium condensation model at constant pressure $p = 1$ bar for Bulk Silicate Earth (BSE) total element abundances. The upper plot shows the condensate-to-gas mass ratio, i.e., the mass of families of condensed species with respect to the mass of the gas. The lower plot shows the relative element abundances in the gas phase on a $\log_{10}$ axis.

2.3 | Why so much sulfur?

The peaking sulfur abundance as function of temperature is a consequence of condensation. From hot to cold temperatures, the relative sulfur abundance first increases, by about two orders of magnitude in the BSE model, as the first Ca-Al-Ti compounds form, as well as some of the most stable liquid silicates and iron-oxides, which drastically reduce the Mg, Si, Fe, Ca, and Al abundances in the gas phase (see Figure 2). At temperatures $\lesssim$ 1170 K in this model, sulfur starts to condense as well, here in the form of FeS[s] (troilite), below which the sulfur abundance in the gas phase falls quickly. Thus, although sulfur is only the 12th most abundant element at high temperatures, it becomes the 3rd most abundant element in the gas between about 1000 K and 2000 K, due to condensation.

At 1500 K, the composition of the atmospheric gas (molar mixing ratios) is 66% H_2O, 19% SO_2, 11% CO_2, 1.5% HCl, 0.64% NaCl, 0.43% HF, and 0.37% KCl, followed by H_2, N_2, CO, and $FeCl_2$, with all other molecules having concentrations < 100 ppm. We note that results like these depend on the completeness of molecular and condensed species included in the model. For example, Fegley et al. (2016) claim that silicic acids is among the species present in a hot steam atmosphere.

At $T \lesssim 650$ K, phyllosilicates and graphite start to become stable in this model, which successively removes all remaining oxygen, hydrogen, and carbon from the gas phase, leaving behind a pure N_2 atmosphere. A condensate to gas mass ratio of 10^6 is reached below about 600 K, which means that 1 gram of gas corresponds to 1 ton of condensates.

The first idea to explain the large range of gaseous sulfur concentrations is to consider the total sulfur (gas and condensed) mass fraction that we use as input. However, we do not see a clear correlation here, see Table B1. For example, the model PWD-BSE with the highest gaseous sulfur abundance has an input sulfur mass fraction of 3.3%, whereas the Earth model, which results in one of the lowest gaseous sulfur concentrations, uses 4.8%.

The amount of sulfur remaining in the gas phase is controlled by the thermal stability of the condensates. In fact, it is the determination of the stable condensates, not the amount of them, that sets the gas phase results. Each stable condensate provides one auxiliary condition to the solution of the gas phase equilibrium, namely that a certain combination of partial pressures must equal the given saturation pressure of that condensate. The amount of each stable condensate can hence be arbitrarily increased without changing the gas phase results, see Appendix B of Woitke et al. (2018).

The most frequent sulfur condensates are found to be FeS[l,s] (trolite), FeS_2[s] (pyrite), $CaSO_4$[s] (anhydrite), and MnS[s] (alabandite), see Table B1. This would suggest that the gaseous S concentration should depend on the availability of Fe and Ca to form those sulfur compounds. The more Fe and Ca was available, the more sulfur condensates should form, which would consume more S and hence lower the S gas concentration. However, this idea also fails to explain our results. All PWD models, for example, use a large input Fe mass fraction of about 10%, whereas the MORB and BSE models use less, 7.3% and 6.3%, respectively; yet the PWD-BSE and PWD-CC models have more gaseous sulfur.

The best explanation we can provide is that it depends on the hierarchy of condensation, that is, how well the most refractory elements, such as Si, Mg, Fe, Al, and Ca, can be put together into highly refractory condensates, which depends on their element stoichiometry. If there is a leftover of Fe or Ca (or, precisely speaking, if it is necessary to put these leftovers into less stable condensates), then sulfur condensates start to form, and the S concentration in the gas phase drops.

More insight into the regulating processes can be obtained by studying the T-dependence shown in Figure 1. We can distinguish between two different cases.

(1) The PWD-BSE, PWD-CC, and PWD-CI models show clear peaks of the sulfur concentration that remain in the gas phase as function of T, and a positive slope in the 1500–3000 K region at 1 bar (the peak value in the PWD-CI model is lower by about a factor of 2–4). At these temperatures, the models show a gradual transition from CO_2 to CO on a $\approx$ 40%-level (see Table B3), an about constant SO_2 concentration, a rising S_2 concentration, and a gradual evaporation of FeS[l] while the FeO[l] concentration rises with increasing temperature. Our conclusion is that the dissociation $CO_2 \rightarrow CO + O$ is followed by $FeS[s] + O \rightarrow FeO[l] + \frac{1}{2}S_2$.
(2) The MORB and BSE models show a constant gaseous sulfur abundance between about 1200 K and 2000 K at 1 bar. These models are featured by a steam atmosphere with high and about constant H_2O-concentration (see Table B3), followed by constant SO_2, CO_2, and O_2 concentrations. There are no stable sulfur condensates at these temperatures, and no CO_2-dissociation, so the gaseous S abundance stays about constant.

Other models show a combination of these two patterns. For example, the CI model at 1 bar first follows the pattern of case (1) up to $\sim$ 1800 K, above which FeS[l] is no longer stable and the gaseous S concentration becomes constant. The CI model has more hydrogen, so H_2O remains the most abundant molecule throughout, and H_2 is present as well. Thus, the release of oxygen as described in case (1) leads to a gradual change of the redox character, causing the H_2S concentration to drop, whereas SO_2 increases, while S_2 is also present.

Changing the gas pressure from 1 bar to 100 bar (see right and left parts of Figure 1) does not change the qualitative behavior of the mixture of gas and condensates. It mainly causes a shift of the thermal stability to higher temperatures such that the temperature thresholds, at which certain phase transitions occur are raised by a factor of roughly 1.3–1.4.

The CC model loses its last sulfur condensate $CaSO_4$[s] at about 900 K at 1 bar, above which there is a constant steam atmosphere made of 44% H_2O and 34% CO_2 with about 5% SO_2, see Table B3. The model with solar input abundances shows a straightforward behavior, with FeS[s] as the main sulfur condensate up to about 650 K at 1 bar, above which there is a constant but low concentration of H_2S, which changes to HS at higher temperatures. Gas giants as investigated by Gao et al. (2017), Hobbs et al. (2021) and Helling et al. (2021) are relevant examples for such A-type atmospheres, see Appendix A. However, the majority of our rocky exoplanet models favors the production of SO_2, which is classified as BC1, BC2, or BC3-type atmospheres in Appendix A.

TABLE 1 The concentration of phosphorus sulfide (PS) at 2000 K and 10 bar. "$\ll$" means a concentration $< 10^{-15}$.

model	PS concentration (ppm)
CC	$\ll$
BSE	$\ll$
CI	2.7
MORB	$\ll$
Archean	1.6
present Earth	$\ll$
PWD-CC	4.3
PWD-BSE	2.9
PWD-CI	260
Solar	3.4×10^{-3}

In the PWD-CC and PWD-BSE models, the molecule S_2 (di-sulfur) also reaches concentrations of a few percent beside the molecule SO_2. Tables B1 and B2 show that these high S_2 concentrations coincide with the peak of the gaseous sulfur abundance around 2500-3500 K shown in Figure 1.

Beside the expected SO_2, H_2S and S_2 molecules, we find smaller concentrations of the molecule PS (phosphorus sulfide) in some of our models, see Table 1. In certain cases, this molecule shows a surprisingly strong absorption feature at optical wavelengths, see Section 3.2.5. In the models using polluted white dwarf abundances, and in the Archean and CI models, the concentrations of PS are between about 1 and several 100 ppm at 2000 K and 100 bar.

In the following section, we explore whether it might be possible to detect sulfur molecules—in particular SO_2, H_2S and PS—by transmission spectroscopy using the James Webb Space Telescope (JWST), given the high sulfur abundances that we predict for hot rocky exoplanets.

3 | TRANSMISSION SPECTRA OF SULFUR-RICH EXOPLANETS

Current and future observational missions like JWST (Benz et al. 2021), LUVOIR, HabEx, and HABITATS (Wang et al. 2020) can be expected to provide an unprecedented quality and variety of transit spectra of diverse rocky exoplanetary worlds. As shown in Tables B1 and B2, our models suggest that some of the atmospheres of these

rocky planets might be very rich in sulfur. Therefore, the question arises whether we can detect sulfur molecules by transmission spectroscopy with present and future observational facilities also for rocky planets. We will not focus on any particular targets, but instead provide a first guidance of where to look for detectable spectroscopic signatures of sulfur-bearing molecules.

3.1 | The model atmosphere

We use simple 1D hydrostatic models with an isothermal structure and constant molecular concentrations. The molecular concentrations are taken from the GGCHEM phase equilibrium models for the surface as described in Section 2. Constant molecular concentrations were previously adopted for atmospheres of magma planets, see, e.g., Barth et al. (2021) and Graham et al. (2021). Strong vertical mixing is expected to occur in such atmospheres, keeping the molecular mixing ratios sustained throughout. We neglect cloud formation.

3.1.1 | The set of opacities in ARCiS

We used ARCiS (Min et al. 2020) to generate transmission spectra. The molecular opacities in these models are determined from standardized pre-computed k-correlations from Chubb et al. (2021), completed with a few species such as H^- (John 1988). The line list data in ARCiS are collected from HITRAN (Gordon et al. 2017), HITEMP (Rothman et al. 2010), MoLLIST (Bernath 2020), ExoMol (Tennyson et al. 2016, 2020) and NIST (Kramida et al. 2013). The ARCiS code has a list of molecules for which opacity data is available, which are:

H^-, Na, K, CH_4, CO_2, H_2O, H_3^+, H_2, VO, TiH, SiH_4, SiH, ScH, SO_3, HS, PS, PH_3, P_2H_2, OH, OH^+, NaF, NaCl, NO, NH, MgO, MgH, MgF, LiH, LiH^+, LiF, LiCl, KCl, H_2S, H_2CO, H_2^+, FeH, CrH, CaO, CaH, CaF, CS, CO, CN, CH_3F, CH_3Cl, AlO, AlH, BeH, AsH_3, AlF, AlCl, TiO, SiS, SO_2, PO, H_2O_2, PN, O_3, O_2, O, C_2, NO_2, NH_3, N_2O, N_2, HCN, HCl, SiO, NS, HNO_3, CH, HF, KF, CP, C_2H_4, C_2H_2.

The line list data of particular importance for this paper can be found in Underwood et al. (2016) for SO_2, in Azzam et al. (2016) for H_2S, in Polyansky et al. (2018) for H_2O, in Li et al. (2015) for CO, in Prajapat et al. (2017) for PS, and in Ygouf et al. (2020) for CO_2 Yurchenko et al. (2020). Table 2 lists some molecules with missing opacity data that could be interesting for hot rocky exoplanet atmospheres.

3.1.2 | Input parameters

The physical input parameters for the ARCiS models are listed in Table 3. We use the hot Super Earth 55 Cnc e as a reference for the stellar and planetary parameters. 55 Cnc e orbits a GV 8 star (Folsom et al. 2020; Tabernero et al. 2020; von Braun et al. 2011), has an equilibrium temperature of 2350 K and a surface pressure of 5 − 10 bar (Hammond & Pierrehumbert 2017). We set the surface pressure to 10 bar and the atmospheric temperature to 2000 K for these simple explorative models, except for those models where we investigate the dependencies on pressure and temperature.

TABLE 2 Atoms and molecules that can be fairly abundant in our atmosphere models without opacity data in ARCiS[a].

$3\% > x > 1\%$	$x > 1\%$	$x > 100$ ppm	$x < 100$ ppm	
NaOH	AlF_2O	Na_2SO_4	Cl	P_2
KOH	COS	H	Mn	S_4
PO_2	P_4O_6	KO	CS_2	SiO_2
S_2O	NaO	S_3	K^+	TiO_2
		HO_2	$(KCl)_2$	$FeCl_2$
		CrO_3	MnH	$Mg(OH)_2$
		$Fe(OH)_2$	K2SO4	$Ca(OH)_2$
		CrO_2	MnO	Cl^-
		$(NaCl)_2$	Fe	Mg

[a] Maximum gas particle concentrations $x = n_{mol}/n_{tot}$ of atoms and molecules across all our atmospheric models with no opacity data in ARCiS, ordered by concentration. We note that KOH and NaOH line lists are now available from Owens et al. (2021).

TABLE 3 Input parameters for our ARCiS spectral models[a].

Parameter	Setting
Effective temperature (star)	5196 K
Stellar radius	0.98 $R_\odot$
Planetary system	55 Cnc e
Atmospheric temperature	2000 K
Surface pressure	10 bar
Planetary radius	1.875 R_{Earth}
Planetary mass	7.99 M_{Earth}
Highest atmospheric layer	10^{-8} bar
No. of atmospheric layers	50
Wavelength range	0.3–29 μm
Spectral resolution	100

[a] Stellar temperature and radius, as well as planetary radius and mass, are taken from estimates for 55 Cnc e, see tab. 1 in Tabernero et al. (2020). By setting the name of the planetary system, these values are automatically adopted by ARCiS. The models use 50 pressure layers for the hydrostatic atmospheric structure. The spectral resolution is set according to the resolution of the MIRI LRS spectrograph on JWST which is tailored to mid infrared spectroscopy.

3.1.3 | Atmospheric composition and extent

The molecular concentrations, taken from the simulations of the near-crust atmospheric composition at p_{surf}, T_{surf} (Section 2), result in very different mean molecular weights, see Table B3, which has an important impact on the observability of the spectral features, because large mean molecular weights translate into compact atmospheres with a small atmospheric extent.

Some of the molecules and atoms, which are included in GGCHEM, are not implemented in ARCiS yet. These molecules are not passed to ARCiS for spectra generation, and are listed in Table 2. Other species are implemented in ARCiS, but have no opacity data there, such as SO and S_2. The absorption features of these molecules cannot be predicted. Ignoring some of the abundant molecules in the ARCiS simulations might have a small impact on the calculation of the mean molecular weight in ARCiS. However, as Table 2 shows, none of these molecules exceeds a concentration of 3%, and the molecules > 1% only occur in our hottest models $T \geq 2500$ K or in the artificially sulfur-enriched models. Among these molecules is NaOH in the Archean and BSE models, for which opacity data have recently been published by Owens et al. (2021) like for the SO molecule. The impact of the mean molecular weight of our models is discussed further in Sections 3.2 and 3.3.

3.1.4 | Pressure broadening and CIA

In our models, the atmospheres of hot rocky exoplanets are mostly constituted of CO_2, H_2O, CO, H_2, and SO_2 (see Table B3). These atmospheres are hence very different from the atmospheres of gas giants where H_2 and He dominate. The opacities we use in this work assume pressure broadening by H_2 and He. The available broadening data of HITRAN2020 (Gordon et al. 2021) for other species indicate that pressure broadening from H_2O in particular is expected to be relevant. Works such as Gharib-Nezhad & Line (2019) and Anisman et al. (2022) illustrate the effect that self-pressure broadening can have for H_2O in steam atmospheres. However, even if we were able to take these pressure broadening effects into account, we do not expect them to affect the main conclusions of the present work. We compute our models considering only collision induced absorption (CIA) from H_2-H_2 and H_2-He. Future work will show whether updated CIA opacities have an influence on these results.

3.2 | Resulting transmission spectra

The following sections show our calculated transmission spectra for 10 different rocky element mixtures and different atmospheric temperatures and surface pressures, see Figure 3 for an overview. In each of these cases, we are looking out for observable spectral features of the various sulfur molecules.

3.2.1 | Mean molecular weight and scale height

The pressure scale height H_p has a profound impact on the observability of spectral features in exoplanet transmission spectra. It is given by

$$H_p = \frac{k_B T}{g\ \mu\ m_H}, \quad (1)$$

where k_B is the Boltzmann constant, T the temperature, $g = GM_{pl}/R_{pl}^2$ the surface gravity of the planet, and μ the mean molecular weight in units of the mass of hydrogen m_H. G, M_{pl}, and R_{pl} are the gravitational constant, the mass, and radius of the planet, respectively, which were adopted from 55 Cnc e (Table 3). In our isothermal models with constant molecular concentrations, we have $T = T_{pl}$ (temperature of the planet's surface and atmosphere), and H_p and μ are constants.

Table B3 lists the results of a series of 10 models with different element abundances at fixed $T = 2000$ K and fixed surface pressure $p_{surf} = 10$ bar. Beside the resulting molecular compositions, we also list the mean molecular weights that vary between 9.2 and 61.6, where the abundant heavy SO_2 molecule can have a profound influence.

Figure 3 shows our predicted transmission spectra for 9 of the 10 models (solar model excluded), where we see a clear correlation between μ and the transit depths. For example, the model with the largest transit depth is the PWD-CI composition. The main species in its atmosphere is H_2 with a mixing ratio of about 67%, followed by H_2O (20%) and CO (8.5%), which results in a mean molecular weight of only $\mu = 9.2$ (Table B3). Larger mean molecular weights μ lead to smaller scale heights H_p, making it more difficult to detect any molecular features by transmission spectroscopy. This effect limits our ability to find and spectroscopically characterize sulfur-rich exoplanets, which generally have large μ.

3.2.2 | SO_2 and H_2S transmission spectroscopy

Table B3 shows that the most abundant gaseous sulfur species in any of our models is either SO_2 or H_2S. Both molecules are nonlinear and polar, with a bent structure similar to H_2O. Whereas SO_2 is more dominant in the BSE,

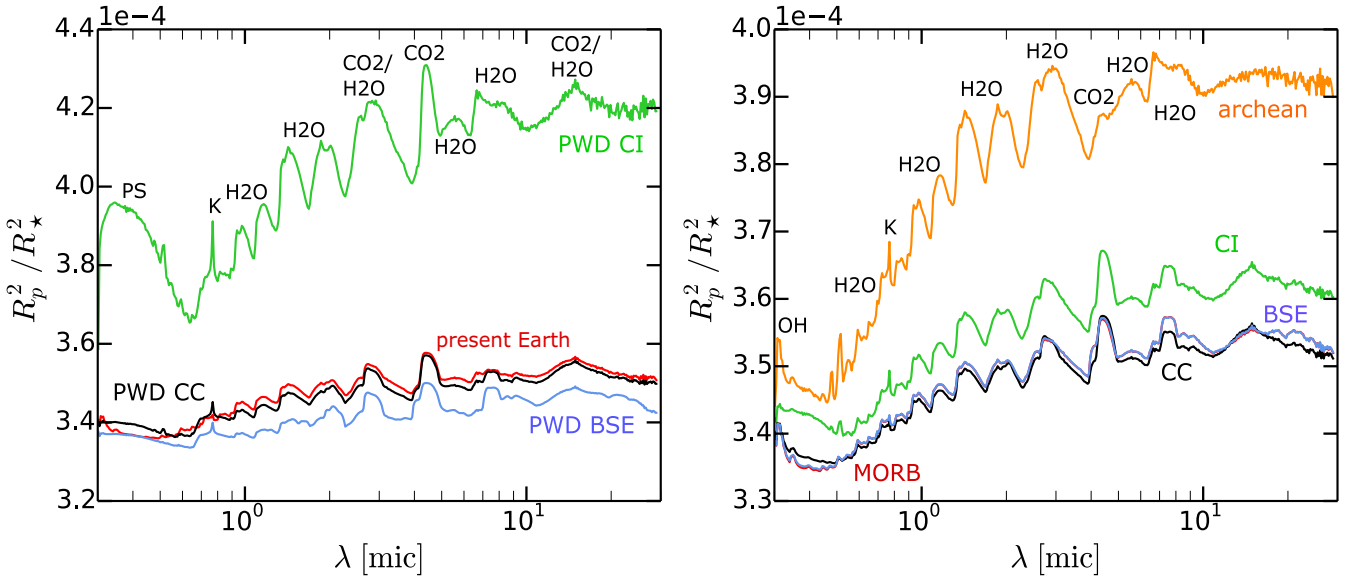

FIGURE 3 Transmission spectra calculated with ARCiS for input parameters listed in Table 3. Nine models with different total element abundances are shown on the left and right. The transmission depths vary according to the different mean molecular weights μ. We note the different scaling of the y-axis on the left and right. All spectra have been computed for a surface pressure of 10 bar and an isothermal atmosphere of 2000 K. The solar model is not shown here because its mean molecular weight $\mu \approx 2.05$, see Table B3, is so small that the transit depth is significantly larger than all other models.

MORB, CC, present Earth, PWD-BSE, and PWD-CC compositions, H_2S dominates in the solar, Archean, CI, and PWD-CI models.

Figures 4 and 5 show the simulated transmission spectra for 2000 K and 10 bar for different total element abundances. From our sample of 10 different rocky element compositions, we have selected the spectra with the most distinct absorption features of SO_2 and H_2S. See Appendix C for all other spectra.

Besides the full spectra based on all included opacities (orange), the figures also show spectra for which the opacities of SO_2 and H_2S have been artificially set to zero (blue). Thus, these molecules are still included in the calculation of the mean molecular weight in ARCiS. The following spectral features of SO_2 and H_2S occur:

- a box-like absorption feature at $7 - 8$ μm with a right shoulder extending to $\sim$ 10 μm $\Rightarrow SO_2$,
- a left shoulder on the main CO_2 absorption band at 4.5 μm $\Rightarrow SO_2$, this is the feature that was recently detected by (Rustamkulov et al. 2023) in WASP 39 b,
- increased absorption longward of 15 μm $\Rightarrow SO_2$.

None of our models predicts strong spectral features of H_2S. Whether H_2S or SO_2 dominates in the gas depends on the O/H ratio in the atmosphere. Our classification scheme for temperatures below 600 K (Appendix A) indicates no coexistence of H_2S and SO_2. However, at larger temperatures, Table B3 shows that both molecules are important in the CI model at 2000 K and 10 bar, indicating a smooth transition from one molecule to the other. At 100 bar, Table B1 indicates that in the CI model, H_2S is abundant below 1700 K and SO_2 at higher temperatures.

3.2.3 | Distinct SO_2 absorption features

SO_2 gives rise to some very distinct spectral features as shown in Figures 4, 5, C1, and C3. These absorption features are particularly strong in the models for MORB, BSE, and PWD-BSE compositions. These are particularly rich in gaseous sulfur as illustrated by Figure 1. The PWD-BSE model provides the sulfur-rich atmosphere, with a sulfur concentration of $\sim$ 15% in the gas phase at 2000 K and 1 bar surface pressure, see Figure 1), which also shows the strongest spectral features due to SO_2 absorption. However, even though the overall gaseous sulfur abundance is the highest there, the SO_2 abundance is not the highest in the PWD-BSE model. Its atmosphere reaches a SO_2 concentration of $\sim$ 14% at 2000 K and 10 bar surface pressure, whereas it is by 4–5% higher for the atmospheres of the BSE and MORB compositions respectively, see Table B3.

This puzzling behavior of the SO_2 absorption features can be explained by looking at the dominant molecular species in the three different atmospheres. While the dominating molecule in the PWD-BSE atmosphere is CO_2, the BSE and MORB atmospheres are mainly composed of H_2O. Water produces very strong absorption features all

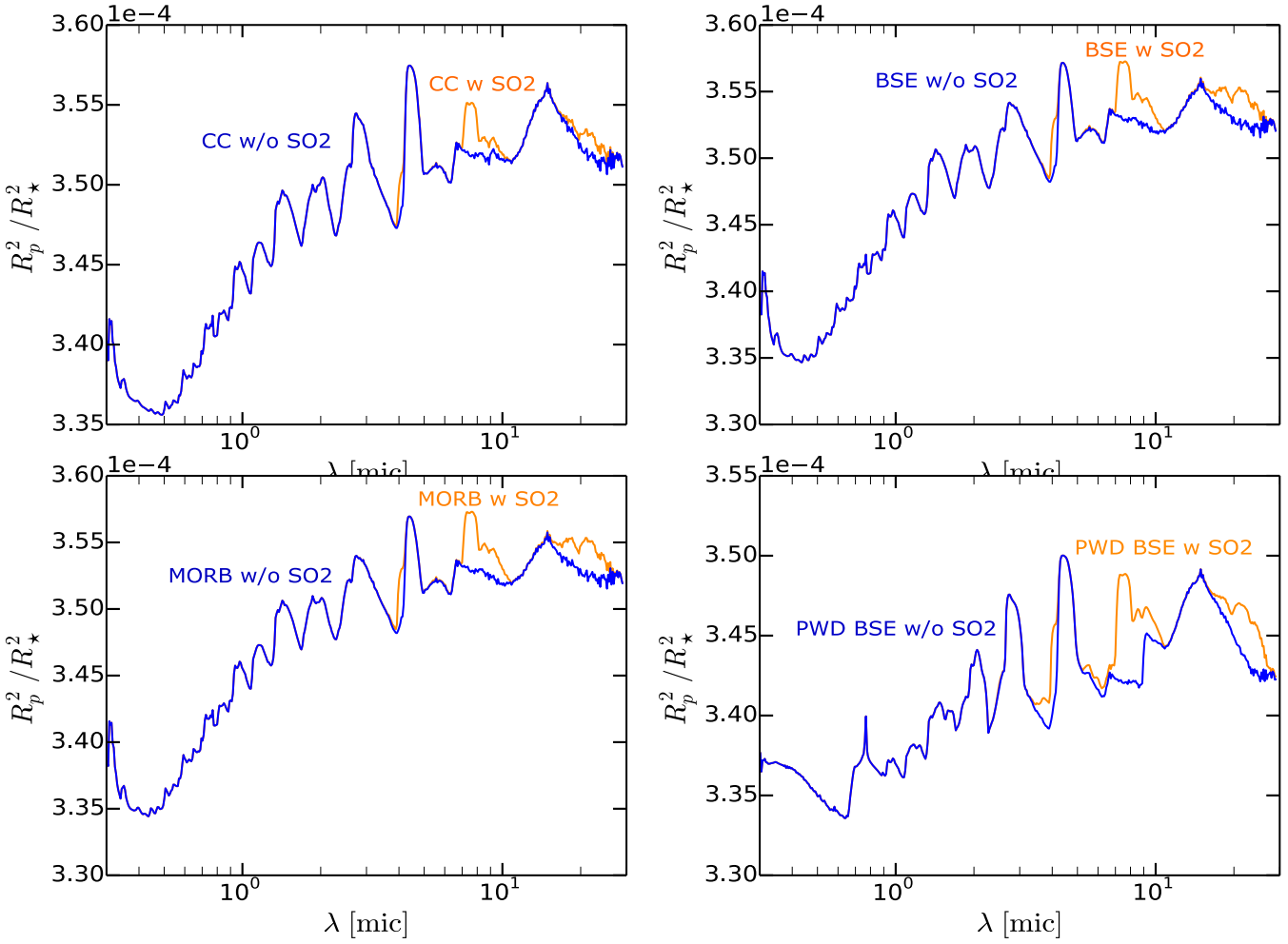

FIGURE 4 Impact of SO_2 on the transmission spectra generated with ARCiS for isothermal atmospheres with $T = 2000$ K and surface pressure $p_{surf} = 10$ bar. The model input parameters are listed in Table 3. The four compositions that show the strongest SO_2 absorption features are selected: CC, BSE, MORB, and PWD-BSE. The blue lines show the spectra when the SO_2 line opacity is omitted.

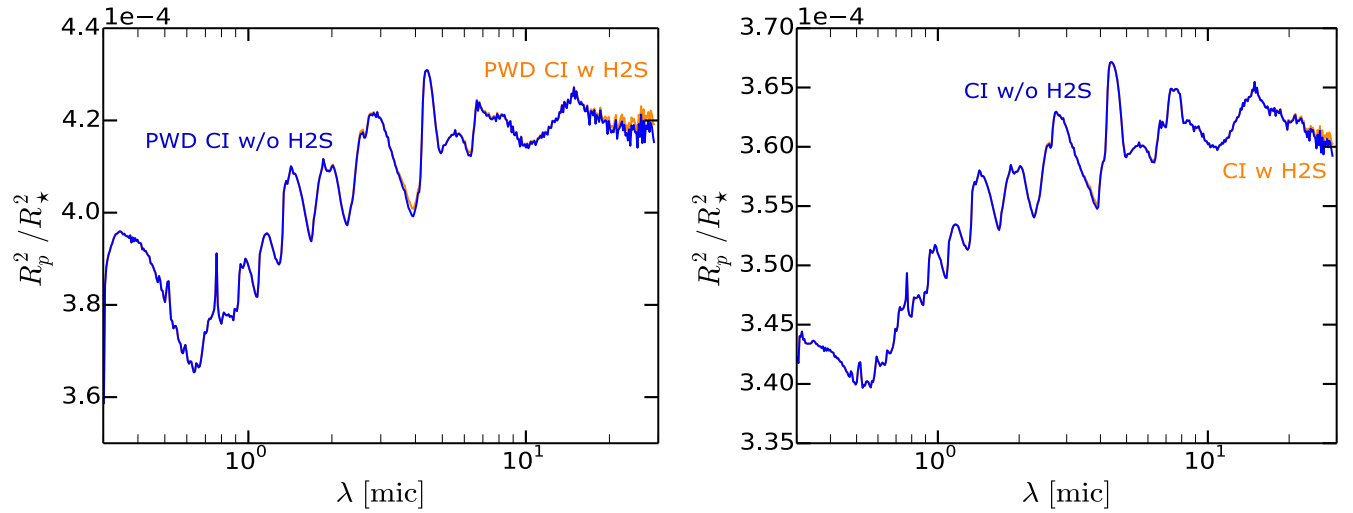

FIGURE 5 Impact of H_2S on the transmission spectra generated with ARCiS for isothermal atmospheres with $T = 2000$ K and $p_{surf} = 10$ bar. The model input parameters are listed in Table 3. The two compositions with visible H_2S features are selected here: CI and PWD-CI. The blue line shows the spectrum when the H_2S line opacity is omitted.

the way between 2 and 10 μm, such that the SO_2 features become undetectable.

3.2.4 | H_2S absorption features

Using ARCiS, we find only weak H_2S absorption features. These features are just about visible in the PWD-CI and the CI models, see Figure 5. CI chondrites found on Earth date back to the time of the evolutionary formation stages of the solar system (Herbort et al. 2020) and are particularly rich in carbon. Besides a high C/O ratio, CI chondrites also have a high H/O ratio. This shows to have a strong impact on the formation of H_2S rather than SO_2. In the CI model, H_2S is the major gaseous sulfur species below 2400 K at 100 bar surface pressure. Above 2400 K, SO_2 becomes the dominant sulfur species even in the CI atmosphere.

The gaseous sulfur concentration in the CI and PWD-CI models is low in comparison with other models such as the BSE composition (see Figure 1), even though the total sulfur abundance for both hydrogen-rich models is high. Therefore, the mixing ratios of all sulfur containing species are relatively low in these two models. The H_2S content reaches 3.6% in the CI model, compared with 19% for SO_2 in the MORB model, which is the model with the largest SO_2 concentration. This is one of the reasons for the shallowness of the H_2S features in Figure 5.

In addition, the H_2S features are located at wavelengths where the H_2O molecule is dominant. The overlap with H_2O opacity is stronger for H_2S than it is for SO_2, such that the water, which dominates in all atmospheres with high H_2S concentrations, masks their features.

3.2.5 | The strong absorption feature of PS

Table 1 shows that all PWD models, the Archean model, and the CI model contain 1–260 ppm of the PS molecule at 2000 K and 10 bar surface pressure. We discovered that this molecule causes a surprisingly strong and broad absorption feature between 0.3 and 0.8 μm, see Figure 6. This figure shows the transmission spectrum of the PWD-CI model, which has the largest PS concentration among all models (260 ppm). The transmission spectra of all other models producing the PS absorption feature are shown in Appendix C.

This unexpected result raises the question about the reliability of the thermochemical data used to calculate the PS concentrations. A comparison of different data sources for the Gibbs free energies of PS (Worters et al. 2017) shows deviations of about 5 kJ/mol, which is a typical uncertainty, so this suspicion can be rejected. According to the NIST database, PS is energetically favored over P_2 and S_2 by about 15 − 20 kJ/mole at about 1500 K.

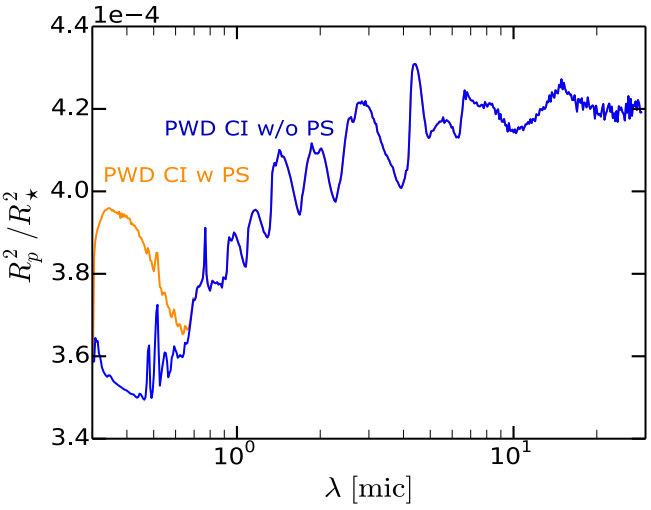

FIGURE 6 Transmission spectrum obtained with ARCiS for PWD-CI abundances at 2000 K and 10 bar. The orange curve shows the complete results including PS, while the blue curve is the spectrum obtained with zero PS opacity.

3.2.6 | Dependence on total sulfur abundance

Considering the BSE composition as an example, we have investigated how the transmission spectrum changes if we arbitrarily vary the total sulfur element abundance in the model. Figure 7 shows spectra for sulfur mass fractions of 0.001, 0.01, 0.027 (unaltered BSE model), 0.1, 0.993 (∼ 1.0), and 4.77 (∼ 5.0)[1].

A larger total element abundance of sulfur allows for more SO_2 and S_2 to form in the gas phase, see Table B3. As both are very heavy molecules, the mean molecular weight of the atmosphere increases, leading to a drop in scale height H_p and therefore to a flattening of all features. This is illustrated in Figure 7. The box-like feature around 7–8 μm of SO_2 is strongest for a total sulfur mass fraction of 0.027%. For smaller values, the SO_2 concentration in the atmosphere drops quickly. For larger values, the radial extent of the atmosphere shrinks substantially, see Table B3.

3.2.7 | The effect of temperature

The temperature affects (i) the equilibrium chemistry in the gas phase, (ii) the phase equilibrium at the planetary

[1]When we set the total element abundance of each individual element (crust and atmosphere) in percentage mass fraction, they do not sum up to exactly 100%. Before computing the equilibrium chemistry, GGCHEM renormalizes to 100%.

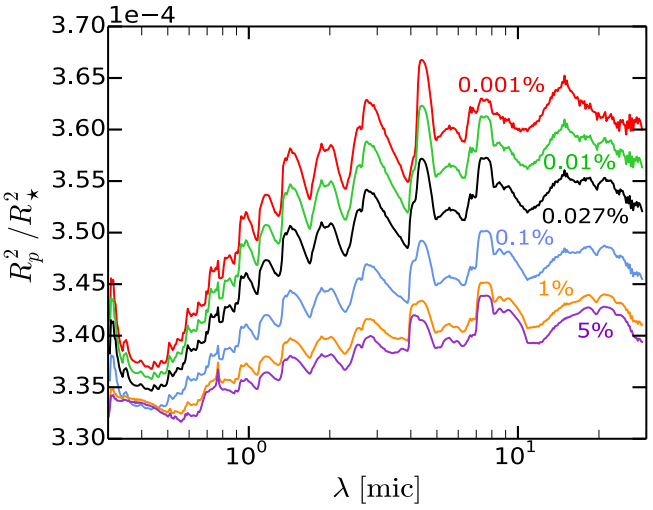

FIGURE 7 Transmission spectra for a Bulk Silicate Earth composition with artificially varied total sulfur element mass fraction (gas and condensates). The spectra have been computed for a surface pressure of 10 bar and an isothermal atmosphere of 2000 K. The numbers next to the graphs indicate the corresponding sulfur mass fraction for each modeled spectrum.

surface, and (iii) the shape of the spectral features as more and more high-excitation lines show up with increasing temperature. As shown in Appendix A, the mixing ratios in a cold atmosphere without condensation are constant up to about 600 K (Woitke et al. 2020). At higher temperatures, the diversity of gaseous species increases such that other sulfur-bearing species occur, for example, COS or SO, in addition to SO_2 or H_2S, see Table B3. But most importantly, the amount of sulfur in the gas is controlled by condensation at the surface, which changes the sulfur content radically.

Figure 8 shows spectra for the BSE model at 1000 K, 2000 and 2500 K. As in Figure C1, the influence of SO_2 is highlighted. At a temperature of 1000 K, the spectral features of SO_2 become almost invisible, which appear clearly in the high-T spectra. This agrees with the predictions in Figure 1, which shows a drastic drop in the gaseous sulfur concentration below $\sim$ 1300 K for the BSE composition with a surface pressure of 100 bar. Less SO_2 can form below this temperature as the condensate FeS builds up.

The overall transit depth, shape, and distinctiveness of the absorption features are affected as well. As the temperature is increased from 1000 K to 2000 K, the SO_2 features appear in the IR wavelength regime, as discussed. At shorter wavelengths, an optical feature of OH at $\sim 0.3-0.4$ μm is present at 2000 K but not at 1000 K. A further increase in temperature from 2000 to 2500 K mainly affects these shorter wavelengths, see Figure 8. The OH peak becomes more distinct and two new peaks appear, as shown in Figure 9. These additional features are due to K (potassium) at $\sim$ 0.8 μm and MgO (Magnesium Oxide) between $\sim$ $0.45-0.8$ μm.

The MgO feature at 2500 K is particularly strong. Magnesium (Mg) is a highly refractory element, which predominantly occurs in condensates. However, as the temperature is increased above $\sim$ 2000 K in the 10 bar model, Mg evaporates to form MgO and MgH.

3.2.8 | Dependence on surface pressure

Figure 10 shows spectra of the BSE model at 2000 K for four different surface pressures between 0.01 and 100 bar. The main effect is a change in the total radial extent of the atmosphere, which increases the overall transit depth. The shape and magnitude of the features is not much affected by the surface pressure between 1 and 100 bar. For much lower pressures, however, other molecular features appear, in particular at shorter wavelengths. The additional peaks in the 0.01 bar spectrum are due to higher concentrations of MgO and K in the gas. This effect is similar to a temperature increase from 2000 to 2500 K at 10 bar surface pressure as discussed in Section 3.2.7.

4 | OBSERVABILITY WITH JWST

In order to investigate the detectability of sulfurous molecules, we use the modeling tool PandExo (Batalha et al. 2017). This allows us to predict the size of the error bars of James Webb Telescope (JWST) measurements for atmospheres of rocky planets. We looked at the NIR regime, which will be covered by the MIRI LRS and NIRCam spectrographs of JWST as well as the MIR regime covered by MIRI MRS.

4.1 | Observability of SO_2 and H_2S

Figures C1–C3 predict that the atmospheric compositions originating from PWD-BSE crust models show the strongest SO_2 features of all our investigated compositions. Therefore, we choose this model to check the observability of SO_2 with JWST.

Figure 11 shows predicted SO_2 observational signatures of this composition assuming a hot equilibrium chemistry atmosphere of 55 Cnc e. The $\sim$ 5 ppm strong SO_2 signal is in principle observable with JWST using NIRSpec/G395M (left) and MIRI/LRS (right) combining 30 and 40 transits, respectively. However, in these calculations, "perfect" performance without systematic noise was assumed.

In general, H_2S is found to show much weaker absorption lines than SO_2 such that it appears quite unlikely that

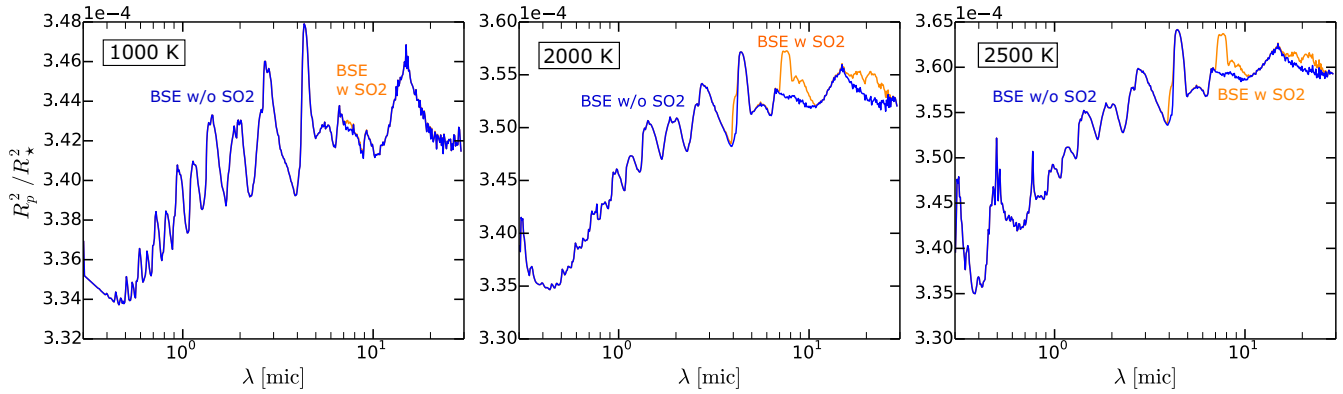

FIGURE 8 Effect of temperature on the spectral appearance of SO_2 in transmission spectra of isothermal atmospheres calculated for BSE total element abundances and a surface pressure of 10 bar.

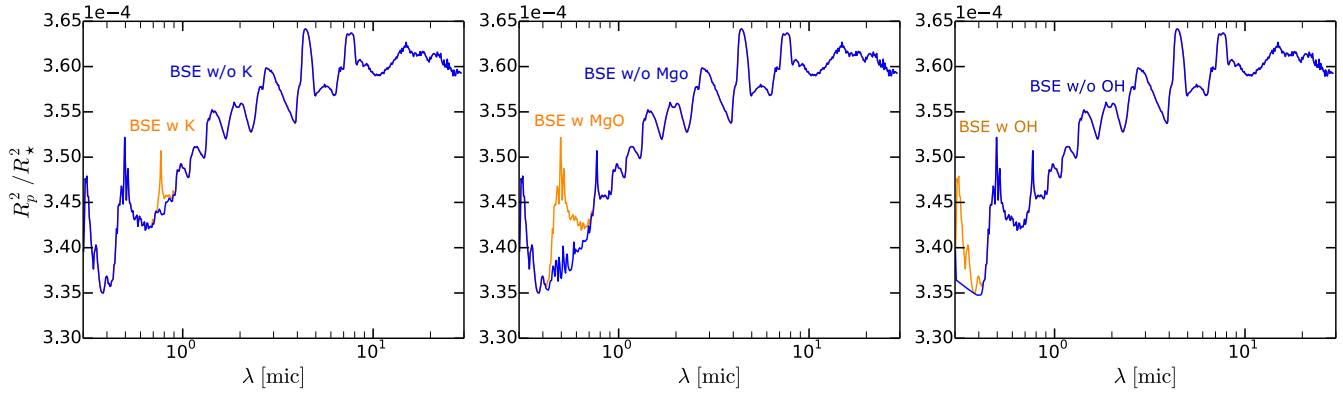

FIGURE 9 Other spectral features in the BSE model with $T_{surf} = 2500$ K and $p_{surf} = 10$ bar.

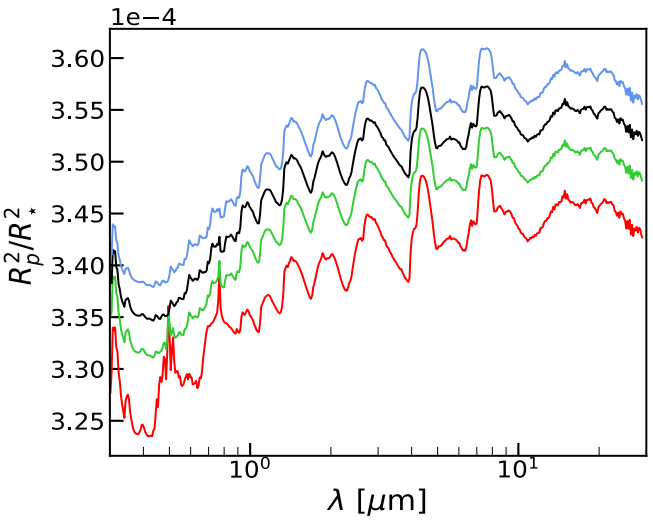

FIGURE 10 Effect of surface pressure on transmission spectra of rocky planets for the BSE model with $T = 2000$ K. The surface pressures are annotated.

present and future missions such as JWST, Ariel, or the Habitable World Observatory (HWO) (Dick et al. 2019; Martin et al. 2020; Ygouf et al. 2020) will be able to detect H_2S in an atmosphere like the one we modeled. The strongest H_2S feature we found is located at long wavelengths in the MIR regime between 20 and 30 μm.

4.2 | Observability of PS

Our ARCiS spectral models show that the molecule PS may cause a broad absorption feature between 0.3 and 0.65 μm that is surprisingly strong (up to ∼ 40 ppm in the PWD-CI chondrite model), despite being based on gaseous PS concentrations of only a few ppm to a few 100 ppm, see Figure C5. The feature's wavelength interval is at the edge of the observable range with JWST. Only NIRSPEC Prism covers the longer wavelength part of this PS feature between 0.6 and 0.65 μm, where it reaches 8 ppm at maximum. Toward shorter wavelengths the feature

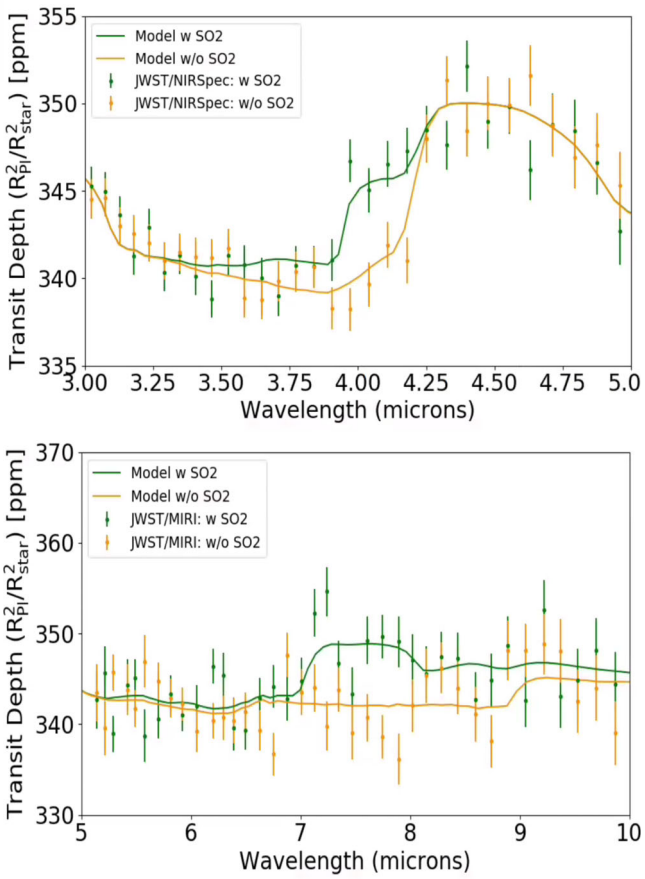

FIGURE 11 Simulated transmission spectra for the PWD-BSE model with SO_2 (green line) and without SO_2 (orange line). Predicted JWST observations are based on combining 30 and 40 transits, respectively, using PandExo (Batalha et al. 2017) for NIRSpec/G395M in the top and for MIRI/LRS in the bottom panel. For clarity, the data was binned down to $R \sim 30$ in their respective wavelength range for both simulated observations.

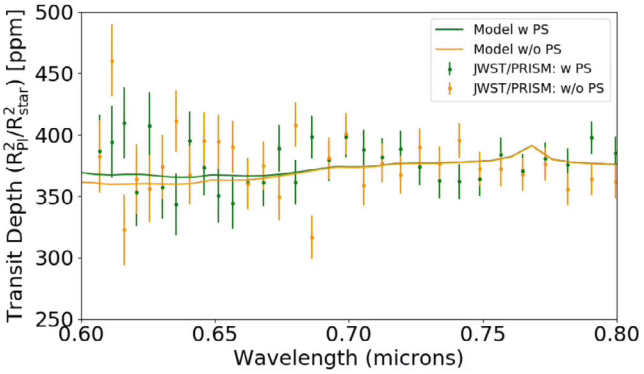

FIGURE 12 Simulated transmission spectrum for the PWD-CI composition with PS (green line) and without PS (orange line). Predicted JWST observations are based on combining 40 transits using PandExo (Batalha et al. 2017). The predictions are for NIRspec/Prism for a system similar to 55 Cnc e with a star of maximal allowed brightness in the J-band of 10.5 mag. A detection of PS does not seem possible. Note the different scaling of the y-axis compared with Figure 11.

strength would increase as predicted in Section 3.2.5, but this is completely out of the detectable range of JWST. In addition, the instrument mode NIRSPEC Prism is only usable for faint stars ($m_J \geq 10.5$). For such targets, the PS feature would not be detectable in any of the compositions according to PandExo predictions, as demonstrated in Figure 12. However, future space telescopes operating at optical wavelengths (0.3–0.6 μm), such as LUVOIR-B, could certainly observe a 40 ppm strong PS feature. Finding PS in a rocky planet atmosphere could also be an interesting science case for ground-based instruments.

4.3 | Dependence on atmospheric structure

We ran a number of additional verification tests where we used more realistic temperature structures for 55 Cancri e. These studies included atmospheric profiles where the temperature is monotonously decreasing with height, similar to fig. 2 of Jindal et al. (2020), and profiles with a temperature inversion, similar to fig. 1 in Zilinskas et al. (2021). In these models, we used GGCHEM to adjust the molecular concentrations to chemical equilibrium at each atmospheric height to the local temperature and pressure, without condensation. While the transition depth and spectral shape of the various absorption features can change substantially in these models, we found that our general conclusions about the detectability of SO_2 and PS in warm and hot rocky exoplanet atmospheres, and the nondetectability of H_2S, remain the same.

5 | SUMMARY AND DISCUSSION

We have investigated how much sulfur can be expected in the atmospheres of warm and hot rocky exoplanets, which sulfur molecules are most abundant, and whether these molecules might be detectable with JWST. A large chemical diversity in planetary environments is expected. We considered various sets of total element abundances, i.e., before condensation, as found in common types of rocks (Herbort et al. 2020; Herbort et al. 2022) and assumed chemical and phase equilibrium at the planetary surface to calculate the chemical composition of the atmospheric gas.

For surface temperatures between about 1000 K and 3000 K, we found typical sulfur concentrations in the gas of a few percent, depending on total element abundances assumed. The most abundant sulfur molecule in the atmosphere, reflecting its redox state, is normally either SO_2 or

H_2S. However, in a few cases, both molecules can coexist beside S_2. Other, less abundant sulfur molecules of interest are SO, SO_3, COS, HS, S_2O, Na_2SO_4, and PS, all of which can occur with concentrations > 100 ppm.

The abundance of sulfur in these atmospheres is controlled by condensation at the surface–atmosphere interface in our models. As sulfur is among the more volatile elements, its gas abundance above 3000 K first increases with falling temperature, as more of the abundant refractory elements like Ca, Al, Ti, Si, Fe, Mn, and Cr condense at the surface. Below about 1000–2000 K, dependent on pressure, sulfur starts to form condensates as well, in particular FeS[s], FeS_2[s], $CaSO_4$[s], MnS[s] and $Na2_2$[s], causing the S abundance in the gas phase to drop quickly. However, at intermediate temperatures, the ability of sulfur to condense, and hence the amount of sulfur left in the gas phase is controlled by the availability of metals such as Fe, Mn, Ca, and Na, which depends on the assumed total element abundances in complicated ways.

In order to determine whether or not the various sulfur molecules might be detectable by transmission spectroscopy, we utilize simple 1D isothermal hydrostatic model with constant molecular concentrations and without clouds. We used the ARCiS modeling platform (Min et al. 2020) to predict such transmission spectra with star-planet system parameters adopted from 55 Cancri e. Based on these models, it seems most promising to search for SO_2 in the atmospheres of hot ($\approx$ 2000 K) rocky exoplanets. SO_2 produces a left shoulder on one of the main CO_2 absorption features at 4.5 μm, a distinct absorption feature at 7–8 μm, and a broad absorption feature at 15–25 μm. These features are most prominent for rocky element abundances derived from polluted white dwarf observations. Quick simulations with PandExo (Batalha et al. 2017) showed that SO_2 might be detectable with JWST in sources like 55 Cnc e, when about 30–40 transits can be observed. In comparison, the molecule H_2S is more difficult to detect. Interestingly, the atmospheres containing lots of sulfur also have large mean molecular weights, and are hence less extended, which limits our ability to detect these molecules in the sulfur-rich atmospheres.

Among all other sulfur species included in our ARCiS models, only the molecule PS is found to be possibly detectable via a strong, broad spectral absorption feature around 0.3–0.65 μm. This could be a case for optical ground-based instruments or LUVOIR, because of JWST's limited possibilities to observe the UV and optical. The NIRspec spectrograph, which we used for our detectability verifications, is only sensitive down to 0.6 micron and designed for faint sources only.

Beside the sulfur molecules SO_2 and PS, we also find detectable absorption features by TiO and MgH in the solar abundance model, and by MgO, OH, and the K resonance line in our hot rocky exoplanet transmission spectra between 0.3 and 0.8 μm, which are otherwise mostly dominated by H_2O and CO_2 absorption. MgO and K are visible only for surface temperatures $\gtrsim$ 2000 K and the OH features becomes more distinct as the temperature rises from 2000 K to 2500 K. We note that ground-based instruments, which can observe high-resolution spectra of exoplanet atmospheres, might allow for the detection of some of these species.

Since the sulfur content in rocky exoplanet atmospheres depends critically on the properties of the planet surface (surface pressure, surface temperature, surface bulk composition), an observational constraint on the SO_2 mixing ratio would be an important step toward a better characterization of the chemical conditions on the planet's surface and habitability.

ACKNOWLEDGEMENTS

P. Woitke, Ch. Helling, M. Min, and L. Carone acknowledge funding from the European Union H2020-MSCA-ITN-2019 under Grant Agreement no. 860470 (CHAMELEON). O.H. acknowledges PhD funding from the St Andrews Center for Exoplanet Science and financial support from the Österreichische Akademie der Wissenschaften. This project has received funding from the EuropeaResearch Council (ERC) under the European Union's 2020 research and innovation programme (grant agreement no. 101088557, N-GINE)

ORCID

L. J. Janssen https://orcid.org/0009-0002-9902-731X

REFERENCES

Allard, F., & Hauschildt, P. H. 1995, *ApJ*, *445*, 433.
Andrews, S. M., Huang, J., Pérez, L. M., et al. 2018, *ApJ*, *869*(2), L41.
Anisman, L. O., Chubb, K. L., Changeat, Q., Edwards, B., Yurchenko, S. N., Tennyson, J., & Tinetti, G. 2022, *J. Quant. Spectrosc. Radiat. Transf.*, *283*, 108146.
Asplund, M., Amarsi, A. M., & Grevesse, N. 2021, *A&A*, *653*, A141.
Asplund, M., Grevesse, N., Sauval, A. J., & Scott, P. 2009, *ARA&A*, *47*(1), 481.
Azzam, A. A. A., Yurchenko, S. N., Tennyson, J., & Naumenko, O. V. 2016, *Mon. Not. R. Astron. Soc.*, *460*, 4063.
Barth, P., Carone, L., Barnes, R., Noack, L., Mollière, P., & Henning, T. 2021, *Astrobiology*, *21*(11), 1325.
Batalha, N. E., Mandell, A., Pontoppidan, K., et al. 2017, *PASP*, *129*(976), 064501.
Benz, W., Broeg, C., Fortier, A., et al. 2021, *Exp. Astron.*, *51*(1), 109.
Bernath, P. F. 2020, *J. Quant. Spectrosc. Radiat. Transf.*, *240*, 106687.
Bonsor, A., Carter, P. J., Hollands, M., Gänsicke, B. T., Leinhardt, Z., & Harrison, J. H. D. 2020, *Mon. Not. R. Astron. Soc.*, *492*(2), 2683.

Calmonte, U., Altwegg, K., Balsiger, H., et al. 2016, *Mon. Not. R. Astron. Soc.*, *462*, S253.
Carone, L., Lewis, D. A., Samra, D., Schneider, A. D., & Helling, C. (2023), arXiv e-prints, arXiv:2301.08492.
Cevallos Soto, A., Tan, J. C., Hu, X., Hsu, C.-J., & Walsh, C. (2022), arXiv e-prints, arXiv:2202.02483.
Chubb, K. L., Rocchetto, M., Yurchenko, S. N., et al. 2021, *AAP*, *646*, A21.
Crossfield, I. J. M. (2023), arXiv e-prints, arXiv:2303.17622.
Dick, S., Li, M., Adams, D., et al. 2019, *AGU Fall Meeting Abstracts Vol. 2019*, P51H. American Geophysical Union, San Francisco, CA.
Dymont, A. H., Yu, X., Ohno, K., Zhang, X., & Fortney, J. J. (2021), arXiv e-prints, arXiv:2112.06173.
Encrenaz, T., Greathouse, T. K., Richter, M. J., et al. 2011, *A&A*, *530*, A37.
Fegley, B., Lodders, K., & Jacobson, N. S. 2023a, *Geochemistry*, *83*(2), 9. Retrieved from https://doi.org/10.1016%2Fj.chemer.2023.125961.
Fegley, J., Bruce, Jacobson, N. S., Williams, K. B., Plane, J. M. C., Schaefer, L., & Lodders, K. 2016, *ApJ*, *824*(2), 103.
Fegley, J., Bruce, Lodders, K., & Jacobson, N. S. 2020, *Chem. Erde-Geochem.*, *80*(1), 125594.
Fegley, J., Bruce, Lodders, K., & Jacobson, N. S. 2023b, *Chem. Erde-Geochem.*, *83*(2), 125961.
Folsom, C. P., Ó Fionnagáin, D., Fossati, L., et al. 2020, *A&A*, *633*, A48.
Gail, H.-P., Keller, R., & Sedlmayr, E. 1984, *A&A*, *133*, 320.
Gao, P., Marley, M. S., Zahnle, K., Robinson, T. D., & Lewis, N. K. 2017, Sulfur hazes in giant exoplanet atmospheres: Impacts on reflected light spectra. Retrieved from https://doi.org/10.3847/1538-3881/aa5fab.
Gao, P., Wakeford, H. R., Moran, S. E., & Parmentier, V. 2021, *J. Geophys. Res. (Planets)*, *126*(4), e06655.
Gharib-Nezhad, E., & Line, M. R. 2019, *Astrophys. J.*, *872*(1), 27.
Gordon, I., Rothman, L., Hargreaves, R., et al. 2021, *JQSRT*, *107949*, 3.
Gordon, I. E., et al. 2017, *J. Quant. Spectrosc. Radiat. Transf.*, *203*, 3.
Graham, R. J., Lichtenberg, T., Boukrouche, R., & Pierrehumbert, R. T. 2021, *Planetary Sci. J.*, *2*(5), 207.
Greene, T. P., Bell, T. J., Ducrot, E., Dyrek, A., Lagage, P.-O., & Fortney, J. J. (2023), arXiv e-prints, arXiv:2303.14849.
Hammond, M., & Pierrehumbert, R. T. 2017, *ApJ*, *849*(2), 152.
Hashimoto, G. L., Abe, Y., & Sugita, S. 2007, *J. Geophys. Res. (Planets)*, *112*(E5), E05010.
He, C., Horst, S., Lewis, N., et al. 2020, *AAS/Division for Planetary Sciences Meeting Abstracts*, Vol. *52*, 403.04.
Helling, C., Lewis, D., Samra, D., et al. 2021, *A&A*, *649*, A44.
Herbort, O., Woitke, P., Helling, C., & Zerkle, A. 2020, *A&A*, *636*, A71 Retrieved from https://doi.org/10.1051/0004-6361/201936614.
Herbort, O., Woitke, P., Helling, C., & Zerkle, A. L. 2022, *A&A*, *658*, A180.
Hobbs, R., Rimmer, P., Shorttle, O., & Madhusudhan, N. (2021), arXiv e-prints, arXiv:2101.08327.
Ito, Y., Ikoma, M., Kawahara, H., Nagahara, H., Kawashima, Y., & Nakamoto, T. 2015, *ApJ*, *801*(2), 144.
Jindal, A., de Mooij, E. J. W., Jayawardhana, R., et al. 2020, *Astron. J.*, *160*(3), 101.
John, T. L. 1988, *A&A*, *193*(1-2), 189.
Kama, M., Shorttle, O., Jermyn, A. S., et al. 2019, *ApJ*, *885*(2), 114.
Khorshid, N., Min, M., Désert, J. M., Woitke, P., & Dominik, C. (2021), arXiv e-prints, arXiv:2111.00279.
Kolecki, J. R., & Wang, J. (2021), arXiv e-prints, arXiv:2112.02031.
Kramida, A., Ralchenko, Y., & Reader, J. 2013, NIST Atomic Spectra Database Version 5. http://www.nist.gov/pml/data/asd.cfm.
Krasnopolsky, V. A. 2012, *Icarus*, *218*(1), 230.
Le Gal, R., Öberg, K. I., Teague, R., et al. 2021, *ApJS*, *257*(1), 12.
Lellouch, E., McGrath, M. A., & Jessup, K. L. 2007, in: *Io After Galileo: A New View of Jupiter's Volcanic Moon*, eds. R. M. Lopes & J. R. Spencer. Springer, Berlin.
Li, G., Gordon, I. E., Rothman, L. S., et al. 2015, *Astrophys. J. Suppl.*, *216*, 15.
Lodders, K. (2019), arXiv e-prints, arXiv:1912.00844.
Lodders, K., & Fegley, B. 2002, *Icarus*, *155*, 393.
Martin, S., Lawrence, C., Redding, D., et al. 2020, *Society of Photo-Optical Instrumentation Engineers (SPIE) Conference Series*, Vol. *11443*, 114432A.
Melis, C., & Dufour, P. 2016, *Astrophys. J.*, *834*(1), 1.
Min, M., Ormel, C. W., Chubb, K., Helling, C., & Kawashima, Y. 2020, *AAP*, *642*, A28.
Moses, J. I., Zolotov, M. Y., & Fegley, B. 2002, *Icarus*, *156*(1), 76.
Ortenzi, G., Noack, L., Sohl, F., et al. 2020, *Sci. Rep.*, *10*, 10907.
Owens, A., Tennyson, J., & Yurchenko, S. N. 2021, *Mon. Not. R. Astron. Soc.*, *502*(1), 1128.
Polyansky, O. L., Kyuberis, A. A., Zobov, N. F., Tennyson, J., Yurchenko, S. N., & Lodi, L. 2018, *Mon. Not. R. Astron. Soc.*, *480*, 2597.
Prajapat, L., Jagoda, P., Lodi, L., Gorman, M. N., Yurchenko, S. N., & Tennyson, J. 2017, *Mon. Not. R. Astron. Soc.*, *472*, 3648.
Rimmer, P. B., Jordan, S., Constantinou, T., Woitke, P., Shorttle, O., Hobbs, R., & Paschodimas, A. 2021, *PSJ*, *2*(4), 133.
Rothman, L. S., Gordon, I. E., Barber, R. J., et al. 2010, *J. Quant. Spectrosc. Radiat. Transf.*, *111*, 2139.
Rustamkulov, Z., Sing, D. K., Mukherjee, S., et al. 2023, *Nature*, *614*(7949), 659.
Schaefer, L., & Fegley, B. 2007, *Icarus*, *186*(2), 462.
Schaefer, L., Lodders, K., & Fegley, B. 2012, *ApJ*, *755*(1), 41.
Shulyak, D., Lara, L. M., Rengel, M., & Nèmec, N.-E. 2020, *A&A*, *639*, A48 Retrieved from https://doi.org/10.1051/0004-6361/201937210.
Speedie, J., Pudritz, R. E., Cridland, A. J., Meru, F., & Booth, R. A. 2022, *Mon. Not. R. Astron. Soc.*, *510*(4), 6059.
Spencer, J. R., Jessup, K. L., McGrath, M. A., Ballester, G. E., & Yelle, R. 2000, *Science*, *288*(5469), 1208.
Sromovsky, L. A., & Fry, P. M. 2018, *Icarus*, *307*, 347.
Stevenson, K. B., Lewis, N. K., Bean, J. L., et al. 2016, *PASP*, *128*(967), 094401.
Stock, J. W., Kitzmann, D., Patzer, A. B. C., & Sedlmayr, E. 2018, *Mon. Not. R. Astron. Soc.*, *479*(1), 865.
Tabernero, H. M., Allende Prieto, C., Zapatero Osorio, M. R., et al. 2020, *Mon. Not. R. Astron. Soc.*, *498*(3), 4222.
Tennyson, J., Yurchenko, S. N., Al-Refaie, A. F., et al. 2016, *J. Mol. Spectrosc.*, *327*, 73.
Tennyson, J., Yurchenko, S. N., Al-Refaie, A. F., et al. 2020, *J. Quant. Spectrosc. Radiat. Transf.*, *255*, 107228.
Timmermann, A., Shan, Y., Reiners, A., & Pack, A. (2023), arXiv e-prints, arXiv:2307.00914.
Tsai, S.-M., Lee, E. K. H., Powell, D., et al. 2023, *Nature*, *617*(7961), 483.
Tsuji, T. 1973, *A&A*, *23*, 411.

Underwood, D. S., Tennyson, J., Yurchenko, S. N., et al. 2016, *Mon. Not. R. Astron. Soc.*, *459*, 3890.
Visscher, C., Lodders, K., Fegley, J., & Bruce. 2006, *ApJ*, *648*(2), 1181.
von Braun, K., Tabetha, S. B., ten Brummelaar, T. A., et al. 2011, *Astrophys. J.*, *740*(1), 49 Retrieved from https://doi.org/10.1088/0004-637x/740/1/49.
Wang, D., Miguel, Y., & Lunine, J. 2017, *ApJ*, *850*(2), 199.
Wang, W., Zhai, M., Zhao, G., et al. 2020, in: *Space Telescopes and Instrumentation 2020: Optical, Infrared, and Millimeter Wave*, eds. M. Lystrup, M. D. Perrin, N. Batalha, et al., Vol. *11443*, SPIE, 341 Retrieved from https://doi.org/10.1117/12.2563343.
Woitke, P., & Helling, C. 2004, *A&A*, *414*, 335.
Woitke, P., Helling, C., Hunter, G. H., et al. 2018, *Astron. Astrophys.*, *614*.
Woitke, P., Herbort, O., Helling, C., Stüeken, E., Dominik, M., Barth, P., & Samra, D. 2020, *Astron. Astrophys.* http://arxiv.org/abs/2010.12241.
Wood, B. J., Smythe, D. J., & Harrison, T. 2019, *Am. Mineral.*, *104*(6), 844.
Wordsworth, R., & Kreidberg, L. (2021), arXiv e-prints, arXiv:2112.04663.
Worters, M., Millard, D., Hunter, G., Helling, C., & Woitke, P. (2017), *Comparison Catalogue of Gas-Equilibrium Constants (Tech. Rep.)*, University of St Andrews, St. Andrews. https://research-repository.st-andrews.ac.uk/handle/10023/12242.
Ygouf, M., Rocha, G., Beichman, C., et al. 2020, *Society of Photo-Optical Instrumentation Engineers (SPIE) Conference Series*, Vol. *11443*, 114433N.
Yurchenko, S. N., Mellor, T. M., Freedman, R. S., & Tennyson, J. 2020, *Mon. Not. R. Astron. Soc.*, *496*(4), 5282.
Zahnle, K., & Mac Low, M.-M. 1994, *Icarus*, *108*(1), 1.
Zahnle, K., Marley, M. S., Morley, C. V., & Moses, J. I. 2016, *ApJ*, *824*(2), 137.
Zilinskas, M., Miguel, Y., Lyu, Y., & Bax, M. 2021, *Mon. Not. R. Astron. Soc.*, *500*(2), 2197.
Zolotov, M. Y., & Fegley, B. 1999, *Icarus*, *141*(1), 40.

How to cite this article: Janssen, L. J., Woitke, P., Herbort, O., Min, M., Chubb, K. L., Helling, C., & Carone, L. 2023, *Astron.Nachr.*, e20230075. https://doi.org/10.1002/asna.20230075

APPENDIX A. CHEMICAL CLASSIFICATION OF THE CHNOS SYSTEM

Woitke et al. (2020) have classified the chemical composition of cold ($T < 600\,\mathrm{K}$) atmospheres which consist only of the four most abundant elements (C, H, N, and O). This resulted in three distinct atmospheric types. Hydrogen-rich type A atmospheres are characterized by the presence of CH_4, H_2O, NH_3 and (H_2 or N_2). Oxygen-rich type B atmospheres show the presence of O_2, CO_2, H_2O, and N_2, and type C atmospheres show the coexistence of CH_4, CO_2, H_2O, and N_2. All other molecules have only trace concentrations in chemical equilibrium at low temperatures. In this appendix, we build upon this model and extend this characterization to additionally include sulfur. In the low-temperature limit, the bulk of the atmosphere consists of exactly the same number of molecules as the numbers of elements, so for C, H, N, O, and S, we expect five abundant molecules in all cases. The element abundances are then sufficient to determine the atmospheric type. With increasing temperatures, other molecules gain importance due to the entropy term in the Gibbs free energy.

Similarly to Woitke et al. (2020), we find different atmospheric types for the gas phase compositions of the CHNOS system. In Figure A1 the number densities of the most dominant gas phase molecules for a sulfur abundance of $S/(C+H+O+S) = 0.1$ are shown. Hereby, the nitrogen abundance is not taken into account as it does not interfere with the chemistry of the other elements but mainly forms N_2. The emerging atmospheric types are described in the following as well as in Table A1.

Type A: The hydrogen dominated atmospheric, subtypes A1 (with NH_3 and H_2) and A2 (with NH_3 and N_2). These types are the same as in Woitke et al. (2020). Sulfur is present in form of H_2S.

Type B: The oxygen dominated atmospheric types are characterized by the presence of O_2, CO_2 and N_2 in all cases. Subtype B2 has H_2SO_4 and H_2O in addition, whereas the new subtype B1 has no water but H_2SO_4 and SO_3 in addition. Subtype B1 occurs for high S/H ratios.

Type C: The coexistence regime of CH_4, CO_2, H_2O, and N_2 is completed by the presence of H_2S as the major sulfur carrying species.

BC subtypes: With increasing sulfur abundance, four new subtypes emerge between type B and C atmospheres, called BC1–BC4. All of these subtypes show the presence of CO_2 and N_2. None of them contains CH_4, NH_3, O_2 or H_2. Sulfur is present in form of certain combinations of H_2S, S_8, SO_2, SO_3, and H_2SO_4, see Table A1. Thus, the subtypes BC1–BC4 are forming a sequence in redox potential.

As in Woitke et al. (2020), additional atmospheric types occur in principle for very large carbon abundances, where graphite is supersaturated. This includes the new peculiar subtype CG, which is like type C, except that water is replaced by the allotrope S_8. For smaller sulfur abundances, see Figure A2, the parameter space occupied by the new subtypes is shrinking, and in the limiting case of very low sulfur element abundance, the original types A, B, and C are again revealed.

A.1 Boundaries between two atmospheric types

Here, we show how the boundaries of the different atmospheric subtypes are derived. As nitrogen does not interfere with the chemistry of the other elements, we omit

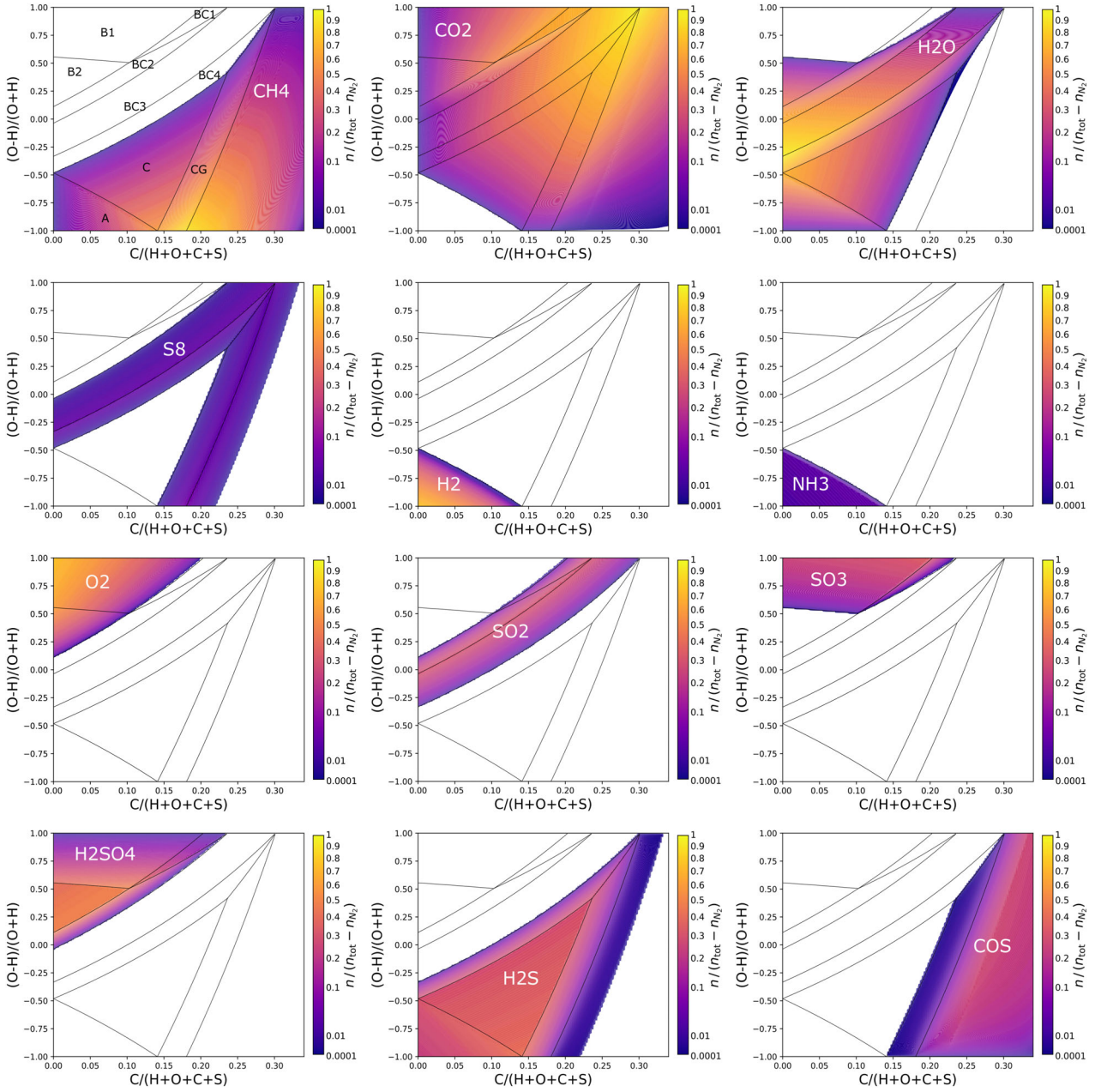

FIGURE A1 Number densities of different molecules for various abundances in the CHNOS system. The N2 abundance is subtracted, as it does only interfere for the type A atmospheres. The solid lines are derived from theoretical calculations as discussed in Section A.1. The colored number densities are a result of equilibrium chemistry calculations with GGCHEM for 300 K and 1 bar. The element abundances of C, H, and O set according to the axis of the plots, while a fixed S abundance is investigated (S/(C+O+H+S) = 0.1). Every subplot shows one distinct molecule.

it for the calculation of the boundaries of the atmospheric types.

At each of these boundaries, the element abundances are such that two molecules replace each other in the adjacent atmospheric types. The other present molecules remain unaltered. The location of the boundary is determined by the condition that

$$p_i > 0. \tag{A1}$$

Here, p_i is the molecular partial pressure of a molecule i, which is present in the investigated atmospheric types.

In the following, we show the derivation of the boundary conditions for atmospheric types on the example of the type C atmosphere, which consists only of the molecules CH_4, CO_2, H_2O, H_2S, and N_2. The fictitious atomic pressure p_{atom} of the gas mixture can be written as

TABLE A1 Classification of atmospheric types including sulfur[a].

Type	H_2	NH_3	N_2	CH_4	CO_2	H_2O	H_2S	S_8	SO_2	SO_3	H_2SO_4	O_2
A1	✓	✓	×	✓	×	✓	✓	×	×	×	×	×
A2	×	✓	✓	✓	×	✓	✓	×	×	×	×	×
B1	×	×	✓	×	✓	×	×	×	×	✓	✓	✓
B2	×	×	✓	×	✓	✓	×	×	×	×	✓	✓
BC1	×	×	✓	×	✓	×	×	×	✓	✓	✓	×
BC2	×	×	✓	×	✓	✓	×	×	✓	×	✓	×
BC3	×	×	✓	×	✓	✓	×	✓	✓	×	×	×
BC4	×	×	✓	×	✓	✓	✓	×	×	×	×	×
C	×	×	✓	✓	✓	✓	✓	×	×	×	×	×
CG	×	×	✓	✓	✓	×	✓	✓	×	×	×	×

[a]In the low-temperature limit, only five molecules coexist in chemical equilibrium with mixing ratios exceeding trace abundances. The three main types are A for hydrogen-rich, B for oxygen-rich, and C for atmospheres where H_2O, CH_4, CO_2, and N_2 can coexist Woitke et al. (2020). By including sulfur, four new sub-types occur between B and C, the BC sub-types, and a fifth sub-type between C type and the graphite condensation zone, named the CG sub-type.

$$p_{\text{atom}} = 3\, p_{\text{H}_2\text{O}} + 5\, p_{\text{CH}_4} + 3\, p_{\text{CO}_2} + 3\, p_{\text{H}_2\text{S}}. \tag{A2}$$

This atomic pressure can further be written in terms of the partial atomic pressures of the CHOS elements with

$$H \cdot p_{\text{atom}} = p_{\text{H}_2\text{O}} + 4p_{\text{CH}_4} + 2p_{\text{H}_2\text{S}}, \tag{A3a}$$

$$C \cdot p_{\text{atom}} = p_{\text{CH}_4} + p_{\text{CO}_2}, \tag{A3b}$$

$$O \cdot p_{\text{atom}} = 2p_{\text{H}_2\text{O}} + 2p_{\text{CO}_2}, \tag{A3c}$$

$$S \cdot p_{\text{atom}} = p_{\text{H}_2\text{S}}, \tag{A3d}$$

where the element abundances H, C, O, and S are normalized by

$$H + C + O + S = 1. \tag{A4}$$

The total gas pressure of the system is given by the sum of all individual molecular partial pressures,

$$p_{\text{gas}} = p_{CO_2} + p_{H_2O} + p_{CH_4} + p_{H_2S}. \tag{A5}$$

One can use Equations (A3a)–(A3d) and Equation (A5) to solve for the molecular partial pressures in terms of element abundances, which leads to

$$\frac{p_{CO_2}}{p_{\text{gas}}} = \frac{4C - H + 2O + 2S}{2H + 4O + 4S}, \tag{A6a}$$

$$\frac{p_{H_2O}}{p_{\text{gas}}} = \frac{-4C + H + 2O - 2S}{H + 2O + 2S}, \tag{A6b}$$

$$\frac{p_{CH_4}}{p_{\text{gas}}} = \frac{4C + H - 2O - 2S}{2H + 4O + 4S}, \tag{A6c}$$

$$\frac{p_{H_2S}}{p_{\text{gas}}} = \frac{4S}{H + 2O + 2S}. \tag{A6d}$$

This shows clearly that sulfur interferes with the chemistry of the C—H—N—O system. Nitrogen, however, stays independent.

The boundary equations can be derived from Equation (A6), by requiring non-negative, nonzero partial pressures of the individual molecules. This leads to

$$\text{a)}\quad H > 4C + 2O + 2S, \tag{A7a}$$

$$\text{b)}\quad 2C + S > O + 0.5H, \tag{A7b}$$

$$\text{c)}\quad O + S > 2C + 0.5H. \tag{A7c}$$

where:

a) no CO_2 exists in the atmosphere
b) no H_2O exists in the atmosphere
c) no CH_4 exists in the atmosphere

Beyond each of these boundaries, a new type of atmosphere will occur. Figure A1 illustrates these boundaries in the C—H—O plane for a constant value of S. Each subfigure shows the occurrence of one particular molecule as a function of (O-H)/(O+H) and carbon fraction (C/(C+H+O+S)) in the gas phase. The considered species are the molecules dominating the atmosphere due

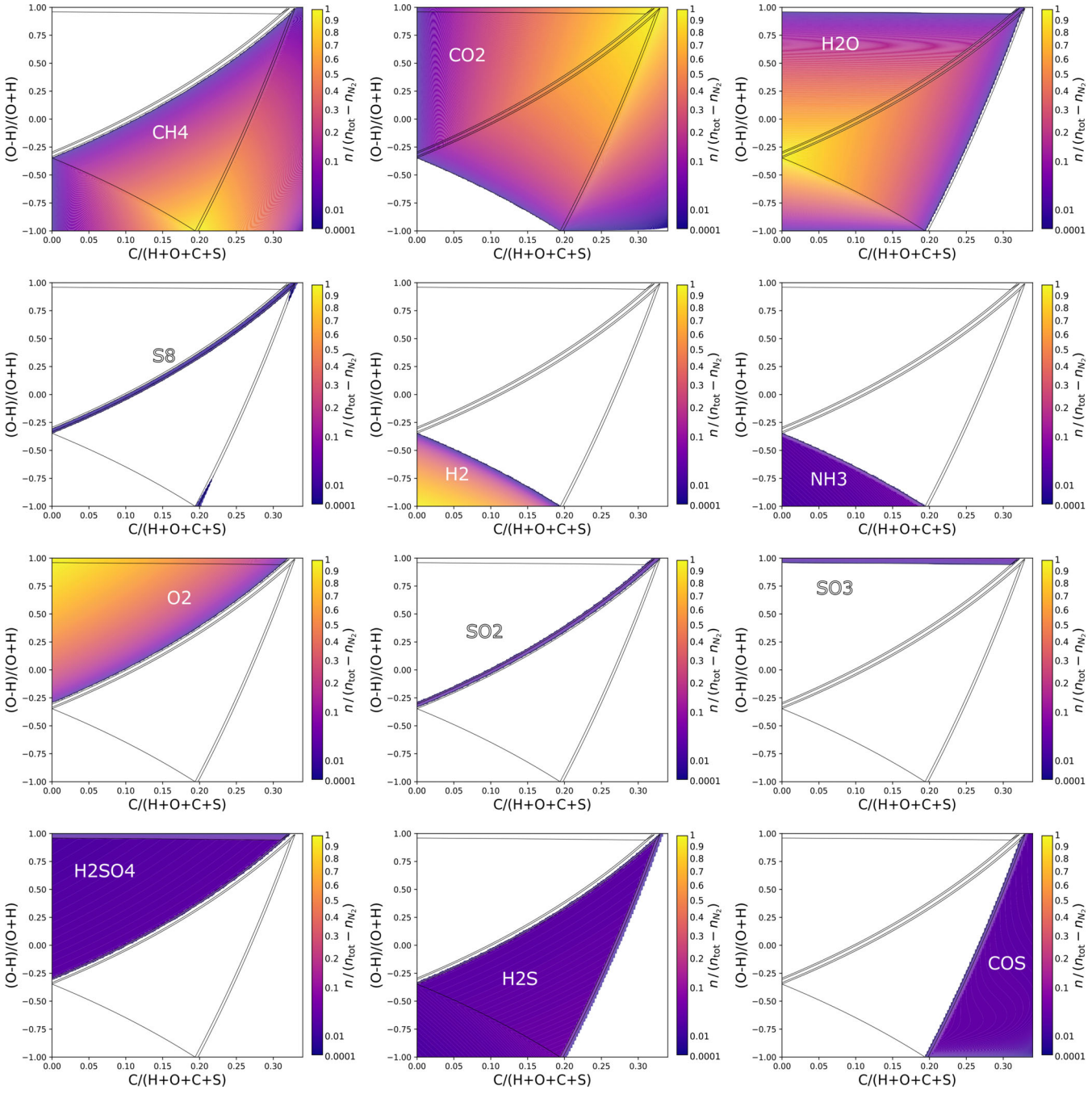

FIGURE A2 As Figure A1, but for S/(C+H+O+S) = 0.01.

to equilibrium at low temperatures. At each black line, which is one of the above mentioned boundaries, the element ratios become such that two molecules replace each other.

A.2 Condensation at low temperatures

In the low-temperature limit, it is subtype specific, which condensates can form. Table A2 lists all of the seven condensates and indicates which of them can form in which subtype. Highly oxidized CHNOS atmospheres such as Earth or Venus will form H_2O[l,s] or H_2SO_4[l,s] depending on sulfur abundance, pressure, and temperature. The atmospheric type of Earth is the B-type (Woitke et al. 2020). However, not enough about the atmospheric chemistry of Venus is known in order to determine its exact type. Since gaseous water is certainly present in Venus'

TABLE A2 Condensates occurring in the various atmospheric types of the CHNOS system at low temperatures.

Type	H_2O[l,s]	H_2SO_4[l,s]	S[l,s],S_2[s],S_8[s]	NH_4SH[s]	C[s]
A1	✓	×	×	✓	×
B1	×	✓	×	×	×
B2	✓	✓	×	×	×
BC1	×	✓	×	×	×
BC2	✓	✓	×	×	×
BC3	✓	✓	✓	×	×
BC4	✓	✓	✓	×	×
C	✓	×	✓	✓	✓
CG	✓	×	✓	×	✓

atmosphere, it is not type BC1. If gaseous H_2SO_4 occurs beside SO_2, Venus would be type BC2. If gaseous S_2 or S_8 occur beside SO_2 it would be type BC3. The gas giants in our Solar System have more reduced atmospheres. Jupiter's atmospheric type is known as an A-type with the corresponding sulfur condensate being NH_4SH[s]. Predicting models for formation of the latter in Jupiter's atmosphere exist (Visscher et al. 2006); however, it has never been confirmed by observations (Sromovsky & Fry 2018).

APPENDIX B. TABLES OF RESULTING GAS PHASE ABUNDANCES

Table B1 lists the major molecules and maximum sulfur fractions in the gas over different rock materials at 100 bar, together with some specifics about the temperature dependencies. Table B2 does the same for 1 bar. Table B3 shows the major molecules with concentrations $> 1\%$ and trace species with concentrations $> 0.1\%$, > 100 ppm, and > 10 ppm, respectively, for different rock materials, temperatures and pressures. Table B4 explains the condensate families used in Figure 2 as a reference.

APPENDIX C. TRANSMISSION SPECTRA

C.1 SO_2 and H_2S

This section shows the transmission spectra generated with ARCiS for all the element compositions which we selected: present Earth, Archean Earth, solar, BSE, MORB, CC, CI, PWD-BSE, PWD-CC and PWD-CI. Figures C1–C4 put the spectra of specific compositions discussed in the main text (BSE and PWD-BSE and MORB for SO_2 and CI and PWD-CI for H_2S) into a wider context by comparing them to the spectra of atmospheres resulting from different types of possible rocky compositions. The figures suggest that H_2S is indeed difficult to detect in warm rocky planet atmospheres.

C.2 PS

Figure C5 compares the PS absorption features of the Polluted White Dwarf compositions. While for the PWD-CI composition, the absorption feature around 0.3–0.8 μm reaches 40 ppm, the feature strength reaches 5 ppm at most in the other compositions. Apart from the low oxygen abundance in the PWD-CI model, it is to note that the scale height in this composition is particularly large, which could be one of the causes for this result. No PS feature can be observed in the solar like composition at all.

TABLE B1 Results of our chemical and phase equilibrium models for different element compositions at 100 bar[a].

Model	Major molecules $n/n_{tot} > 10^{-1.5}$ with T-range (K)	$\epsilon_S^{gas+cond}$ (% mf)	max. ϵ_S^{gas} / $\sum_k \epsilon_k^{gas}$ (mol. fractions)	T-range (K) with high ϵ_S^{gas}[a] T (K) at ϵ_S^{gas}-max.	Type[b] at 600K	Most abundant[c] sulfur molecules and T-range (K)	Condensed sulfur species and T-range (K)
CC	220–630: N_2 620–3930: H_2O 510–3950: CO_2 1120–3220: SO_2 2070–5000: O_2	0.07	0.0176	1110–3770 1150	C	H_2S: 200–800 SO_2: 800–4600 SO: ≥4600	≤640: FeS_2[s] 650–1150: $CaSO_4$[s]
CI	260–550: N_2 1780–2470: H_2S 2310–4110: SO_2 410–5000: H_2O 490–4060: CO_2 390–720: CH_4 1350–5000: CO 830–5000: H_2	5.411	0.0448	1920–4220 2310	C	H_2S: 200–2400 SO_2: 2400–4300 SO: ≥4300	≤520: FeS_2[s] 480–1480: FeS[s] 1500–2220: FeS[l] 2160–2280: MnS[s]
BSE	≤780: N_2 750–3690: H_2O 1270–3670: SO_2 2840–4140: NaOH 690–3360: CO_2 2190–5000: O_2	0.027	0.0662	1290–2250 1320	C	H_2S: ≤1200 SO_2: 1200–4600 SO: ≥4600	≤1310: FeS[s]
MORB	≤660: N_2 620–3950: H_2O 580–3580: CO_2 1230–3930: SO_2 2780–5000: O_2	0.110	0.0707	1280–3750 1310	C	H_2S: ≤1200 SO_2: 1200–4600 SO: ≥4600	≤1300: FeS[s]
Solar	100–5000: H_2	0.041	$1.31 \cdot 10^{-5}$	≥650 1140	A1	H_2S: ≤3600 HS: 3600–4800 S: ≥4800	FeS[s] < 10^{-4} MnS[s] < 10^{-4}
Archean Earth	411–5000: H_2O 100–5000: H_2 CH_4 reaches peak abund. of $n/n_{tot} = 10^{-2.96}$ only	0.027	0.00024	650–4160 700	A1	H_2S: ≤3150 SO_2: 3150–4400 SO: ≥ 4400	≤ 660: FeS[s]

TABLE B1 (Continued)

Model	Major molecules $n/n_{tot} > 10^{-1.5}$ with T-range (K)	$\epsilon_S^{gas+cond}$ (% mf)	max. $\epsilon_S^{gas} / \sum_k \epsilon_k^{gas}$ (mol. fractions)	T-range (K) with high ϵ_S^{gas}[a] T (K) at ϵ_S^{gas}-max.	Type[b] at 600K	Most abundant[c] sulfur molecules and T-range (K)	Condensed sulfur species and T-range (K)
Earth	700–770: NH_3	4.841?	0.0165	≥2810	B1	H_2SO_4: ≤900	≤1540: MgS[s]
	130–1760: CH_4			3160		SO_3: 900–950	≤2340: CaS[s]
	2440–5000: CO					SO_2: 950–4600	1540–1800: MnS[s]
	100–5000: H_2					SO: ≥4600	
PWD	270–460: NH_3	3.3	0.0392	2570–4060	A1	H_2S: ≤3400	≤ 2530: MnS[s]
CI	2470–3160: H_2S			3000		HS: 3400–3800	≤ 1480: FeS[s]
	130–1330: CH_4					SO: ≥3800	1500–2960: FeS[l]
	490–5000: H_2O						
	1270–4060: CO						
	100–5000: H_2						
PWD	510–3120: H_2O	3.3	0.1611	2890–4110	C	H_2S: ≤2300	970–2700: MnS[s]
CC	630–3330: CO_2			3420		SO_2: 2300–2500	210–1480: FeS[s]
	470–750: CH_4					S_2: 2500–3500	1500–3330: FeS[l]
	2850–4500: Na					SO: ≥3500	≤280: FeS_2[s]
	900–4500: SO						3420–3250: Na_2S[s]
	2700–3650: S_2						
	100–560: N_2						
	930–3080: H_2						
PWD	100–690: N_2	3.3	0.2425	2370–4110	C	H_2S: ≤800	810–1030: $CaSO_4$[s]
BSE	1540–4750: CO			3290		SO_2: 800–2900	350–1480: FeS[s]
	570–4270: CO_2					S_2: 2900–3500	≤800: FeS_2[s]
	2600–4330: SO					SO: ≥3500	1500–3290: FeS[l]
	1270–4330: SO_2						2220–2700: MnS[s]
	2080–3850: S_2						2220–2700: MnS[s]

[a]The total (gas and condensate) sulfur abundances $\epsilon_S^{gas+cond}$ (input) are listed in mass fraction percentages (% mf). The sulfur element abundances in the gas phase $\epsilon_S^{gas} / \sum_k \epsilon_k^{gas}$ (output) are given in molar fractions, i.e. number of S-nuclei divided by the sum of the numbers of nuclei of all elements, where ϵ_S^{gas} is at least $\frac{1}{2}$ of its maximum.

[b]The atmospheric type of the model, see Appendix A1.

[c]Considering $T < 3000$K.

TABLE B2 Results of our chemical and phase equilibrium models for different element compositions at 1 bar[a].

Model	Major molecules $n/n_{tot} > 10^{-1.5}$ with T-range (K)	$\epsilon_S^{gas+cond}$ (% mf)	max. ϵ_S^{gas} / $\sum_k \epsilon_k^{gas}$ (mol. fractions)	T-range (K) with high ϵ_S; T (K) at ϵ_S^{gas}-maximum	Type at 600K	Most abundant sulfur molecule: T-range (K)	Condensed sulfur species in crust with T-range (K)
CC	100–500: N_2 500–2900: H_2O 400–2900: CO_2 900–2400: SO_2 1750–4300: O_2 2650–2800: OH 1050–1700: HF 2800–3100: K	0.07	0.0175	1110–3770 890	C	H_2S: ≤1000 SO_2: 1000–3600 SO: 3600–4000 S: ≥4000	650–880: $CaSO_4$ (s) ≤640: FeS_2[s]
CI	100–370: N_2 2850–4200: OH 1800–3200: SO_2 300–3700: H_2O 400–3100: CO_2 280–550: CH_4 1300–5000: CO 600–3900: H_2	5.411	0.0450	1920–4220 1800	C	H_2S: ≤1700 SO_2: 17,000–3400 SO: 3400–4000 S: ≥4000	≤460 FeS_2[s] 460–1480: FeS[s] 1500–1780: FeS[l]
BSE	≤650: N_2 600–3050: H_2O 1150–2700: SO_2 600–2550: CO_2 1900–4300: O_2 700–800: H_2	0.027	0.0658	1290–2250 1200	C	H_2S: ≤1100 SO_2: 1000–3500 SO: 3500–4000 S: ≥ 4000	≤1170: FeS[s]
MORB	≤550: N_2 500–2850: H_2O 500–2700: CO_2 1050–2800: SO_2 1900–4300: O_2 2700–2800: OH 2700–2800: K	0.110	0.0703	1280–3750 1100	C	H_2S: ≤1000 SO_2: 1000–3600 SO: 3600–4000 S: ≥4000	≤1100: FeS[s]
solar	100–4800: H_2 2600–5000: H	0.041	$1.31 \cdot 10^{-5}$	≥650 1300	A1	H_2S: 100–2600 HS: 2600–3100 S: ≥3100	

TABLE B2 (Continued)

Model	Major molecules $n/n_{\rm tot} > 10^{-1.5}$ with T-range (K)	$\epsilon_{\rm S}^{\rm gas+cond}$ (% mf)	max. $\epsilon_{\rm S}^{\rm gas}$ / $\sum_k \epsilon_k^{\rm gas}$ (mol. fractions)	T-range (K) with high $\epsilon_{\rm S}$; T (K) at $\epsilon_{\rm S}^{\rm gas}$-maximum	Type at 600K	Most abundant sulfur molecule: T-range (K)	Condensed sulfur species in crust with T-range (K)
Archean Earth	300–3750: H_2O 100–3950: H_2 2850–4200: OH CH_4 reaches peak abund. of $n/n_{\rm tot} = 10^{-2.98}$ only	0.027	0.0024	650–4160	A1	H_2S: ≤2100 SO_2: 2100–3400 SO: 3400–4400 S: ≥4400	Fes[s]: 100–650
Earth	100–370: N_2 300–3150: H_2O 350–3150: CO_2 100–4200: O_2 2450–5000: CO 2650–3650: OH 2800–3000: K	4.841?	0.0165	≥2810	B1	$H_2 2SO_4$: ≤650 SO_3: 650–8000 SO_2: 800–3600 SO: 3600–4000 S: ≥4000	≤1170: $CaSO_4$[s]
PWD CI	200–350: NH_3 2650–5000: H 100–950: CH_4 400–3650: H_2O 900–3100: CO 100–3900: H_2	3.3	0.0399	2570–4060 2300	A1	H_2S: ≤2400 S_2: 2400–2500 HS: 2500–3700 SO: 3700–3900 S: ≥3900	≤1500: FeS[s] ≤2080: MnS[s] 1500–2250: FeS[l]
PWD CC	400–2250: H_2O 500–3150: CO_2 400–700: CH_4 2100–3250: K 2450–3100: SO 1950–2750: S_2 100–450: N_2 650–2250: H_2 2250–3300: SO_2 750–3300: CO	3.3	0.1746	2890–4110 2400	C	H_2S: ≤1700 S_2: 1700–2600 S_2: 2600–2800 SO_2: 2800–3500 SO: 3500–4000 S: ≥ 4000	210–1480: FeS[s] 1500–2370: FeS[l] ≤280: FeS_2[s] 900–2250: MnS[s]
PWD BSE	100–550: N_2 1300–3300: CO 450–3200: CO_2 2150–3200: SO 1150–3300: SO_2 1550–2850: S_2	3.3	0.2586	2370–4110 2400	C	H_2S: ≤700 SO_2: 700–2000 and 2900–3500 S_2: 2000–2700 SO: 3600–4000 S: ≥4000	≤800: FeS_2[s] 350–1480: FeS[s] 1500–2370: FeS[l] 2220–2340: MnS[s] 810–830: $CaSO_4$[s]

[a]Like Table B1 but for a surface pressure of 1 bar, where the sulfur abundance is at $\frac{1}{2}$ of its maximum.

TABLE B3 Molecular composition of the atmospheric gas in our rocky exoplanet models with varying element composition, surface temperature, and pressure. Sulfur molecules are highlighted in bold face.

Model	$n_{mol}/n_{tot} \geq 1\%$ (%)	$\geq 0.1\%$ (%)	≥ 100 ppm (ppm);	≥ 10 ppm (ppm)	μ (amu)
CC	H_2O: 44	AlF_2O: 0.90	NaF: 590	$(NaCl)_2$: 84	
2000 K	CO_2: 34	HCl: 0.74	NaOH: 490	O: 69	32.155
10 bar	O_2: 11	KCl: 0.62	CO: 430	$FeCl_2$: 64	
	SO_2: 4.5	N_2: 0.42	NO: 420	$(KCl)_2$: 23	
	HF: 2.2	OH: 0.21	KF: 330	HO_2: 12	
	NaCl: 1.3		**SO_3: 270**		
			Cl: 250		
			KOH: 210		
			$Fe(OH)_2$: 150		
			H_2: 120		
CI	H_2O: 55	N_2: 0.77	NaCl: 940	K: 86	
2000K	H_2: 13	**HS: 0.39**	Na: 880	OH: 81	23.300
10 bar	CO: 11	**SO: 0.38**	**S_2O: 850**	**S_3: 41**	
	CO_2: 10	NaOH: 0.17	KOH: 540	PO_2: 24	
	H_2S: 3.6	**COS: 0.11**	KCl: 320	NaF: 16	
	SO_2: 3.2		$Fe(OH)_2$: 220		
	S_2: 2.2		HF: 200		
			HCl: 190		
			H: 180		
			S: 150		
BSE	H_2O: 64	KCl: 0.53	N_2: 640	NO: 85	
2000 K	**SO_2: 18**	HF: 0.35	KOH: 580	**Na_2SO_4: 68**	30.853
10 bar	CO_2: 11	HCl: 0.33	**SO_3: 560**	Cl: 68	
	O_2: 2.8	N_2: 0.42	H_2: 350	**SO: 53**	
	NaCl: 1.6	NaOH: 0.19	CO: 270	Na: 43	
		OH: 0.18	$Fe(OH)_2$: 260	O: 35	
			NaF: 250	$(KCl)_2$: 17	
			AlF_2O: 160	$FeCl_2$: 10	
			$(NaCl)_2$: 120		
			KF: 100		
MORB	H_2O: 63	HCl: 0.68	**SO_3: 780**	N_2: 89	
2000 K	**SO_2: 19**	KCl: 0.48	NaOH: 580	$(NaCl)_2$: 51	30.895
10 bar	CO_2: 8.9	OH: 0.21	NaF: 280	O: 47	
	O_2: 4.9	AlF_2O: 0.16	H_2: 260	$FeCl_2$: 44	
	HF: 1.2		$Fe(OH)_2$: 250	NO: 42	
	NaCl: 1.0		KOH: 250	**SO: 42**	
			CO: 170	$(KCl)_2$: 14	
			Cl: 160	Na: 12	
			KF: 150		

TABLE B3 (Continued)

Model	$n_{mol}/n_{tot} \geq 1\%$ (%)	$\geq 0.1\%$ (%)	≥ 100 ppm (ppm);	≥ 10 ppm (ppm)	μ (amu)
Archean	H_2O: 64	NaOH: 0.19	**H_2S: 560**	HF: 73	
2000 K	H_2: 36	Na: 0.14	H: 310	K: 70	12.421
10 bar			KOH: 300	NaCl: 61	
			CO: 270	OH: 56	
			$Fe(OH)_2$: 250	PO_2: 37	
			CO_2: 110	**HS: 36**	
				SO_2: 30	
				NaH: 19	
				HCl: 13	
				KCl: 11	
				PO: 10	
	CO_2: 47	**SO_2: 0.57**	HCl: 970	KF: 65	
Earth	H_2O: 46	HF: 0.44	CO: 890	O: 46	31.386
2000 K	O_2: 4.8	N_2: 0.25	KCl: 800	Cl: 27	
10 bar		OH: 0.18	NaOH: 500	**SO_3: 23**	
		NaCl: 0.17	AlF_2O: 290	Na: 12	
			NO: 220		
			KOH: 210		
			H_2: 190		
			$Fe(OH)_2$: 180		
			NaF: 120		
PWD	H_2: 67	N_2: 0.95	**HS: 950**	**COS: 92**	
CI	H_2O: 20	CO_2: 0.55	K: 420	NaH: 87	9.2369
2000 K	CO: 8.5	Na: 0.45	H: 420	PO_2: 86	
10 bar	**H_2S: 2.0**	P_4O_6: 0.15	KCl: 410	Mn: 63	
		NaOH: 0.14	KOH: 410	$Fe(OH)_2$: 51	
		NaCl: 0.13	**PS: 260**	MnH: 48	
			S_2: 250	NaF: 39	
			HF: 220	Fe: 37	
			PO: 140	**SO: 28**	
			PN: 120	P_2: 18	
			HCl: 110	**S: 16**	
				SO_2: 15	
				KF: 15	
				SiO: 14	
				OH: 13	
				NH_3: 11	

TABLE B3 (Continued)

Model	$n_{mol}/n_{tot} \geq 1\%$ [%]	≥ 0.1% [%]	≥ 100 ppm [ppm];	≥ 10 ppm [ppm];	mean molecular weight [amu]
PWD	CO: 47	H_2S: 0.8	NaF: 390	$Fe(OH)_2$: 49	
CC	CO_2: 31	KCl: 0.72	**S_2O: 280**	OH: 32	32.187
2000 K	H_2O: 12	**COS: 0.33**	HCl: 200	$(KCl)_2$: 31	
10 bar	H_2: 4.1	NaCl: 0.29	**S: 100**	PO_2: 22	
	S_2: 1.1	KOH: 0.25	H: 100	**S_3: 14**	
	SO_2: 1.0	**SO: 0.18**			
		HF: 0.18			
		N_2: 0.17			
		HS: 0.15			
		Na: 0.14			
		KF: 0.12			
		NaOH 0.11			
		K: 0.10			
PWD	CO_2: 47	**COS: 0.50**	Na: 920	K: 90	
BSE	CO: 30	**S_2O: 0.37**	**H_2S: 730**	PO_2: 36	43.085
2000 K	**SO_2: 14**	H_2: 0.16	**HS: 710**	HF: 34	
10 bar	**S_2: 6.0**		NaCl: 640	NaF: 25	
	H_2O: 1.1		NaOH: 330	N_2: 24	
	SO: 1.0		S: 250	H: 20	
			KCl: 220	OH: 15	
			S_3: 180	HCl: 13	
			KOH: 100	**CS_2: 13**	
				KF: 10	
BSE	H_2O: 79	**SO_2: 0.83**	N_2: 790	NO: 94	
2000 K	CO_2: 13	KCl: 0.64	KOH: 640	Cl: 82	23.615
10 bar	O_2: 2.8	HCl: 0.45	H_2: 430	Na: 43	
$\epsilon_s^{tot} = 0.001$	NaCl: 1.9	HF: 0.43	CO: 330	O: 35	
mass fraction [%]		NaOH: 0.21	$Fe(OH)_2$: 310	**SO_3: 26**	
		OH: 0.20	NaF: 280	$(KCl)_2$: 25	
			AlF_2O: 200	$FeCl_2$: 15	
			$(NaCl)_2$: 170	H: 11	
			KF: 110		
BSE	H_2O: 73	KCl: 0.60	N_2: 730	NO: 91	
2000 K	CO_2: 12	HF: 0.40	KOH: 620	Cl: 77	26.461
10 bar	**SO_2: 7.7**	HCl: 0.40	H_2: 400	Na: 43	
$\epsilon_s^{tot} = 0.01$	O_2: 2.8	NaOH: 0.20	CO: 310	O: 35	

TABLE B3 (Continued)

Model	$n_{mol}/n_{tot} \geq 1\%$ [%]	≥ 0.1% [%]	≥ 100 ppm [ppm];	≥ 10 ppm [ppm];	mean molecular weight [amu]
mass fraction [%]	NaCl: 1.8	OH: 0.19	$Fe(OH)_2$: 290	**Na_2SO_4: 29**	
			NaF: 270	**SO: 22**	
			SO_3: 240	$(KCl)_2$: 21	
			AlF_2O: 180	$FeCl_2$: 13	
			$(NaCl)_2$: 150	H: 10	
			KF: 110		
BSE	**SO_2: 45**	KCl: 0.36	KOH: 470	KF: 81	
2000 K	H_2O: 43	HF: 0.23	N_2: 420	NO: 69	41.824
10 bar	CO_2: 7.2	HCl: 0.19	H_2: 230	$(NaCl)_2$: 56	
$\epsilon_s^{tot} = 0.1$	O_2: 2.8	NaOH: 0.15	NaF: 200	Cl: 46	
mass fraction [%]	NaCl: 1.1	OH: 0.15	CO: 180	Na: 43	
		SO_3: 0.14	$Fe(OH)_2$: 170	O: 35	
			Na_2SO_4: 170	**K_2SO_4: 16**	
			SO: 130		
			(AlF_2O): 100		
BSE	**SO_2: 61**	**H_2S: 0.82**	NaOH: 820	OH: 64	
2000 K	**S_2: 16**	CO: 0.69	**S_3: 800**	H: 53	56.361
10 bar	H_2O: 13	NaCl: 0.39	HF: 780	K: 52	
$\epsilon_s^{tot} = 0.993$	**SO: 2.8**	**HS: 0.30**	Na: 540	KF: 51	
mass fraction [%]	CO_2: 1.8	KCl: 0.13	**S: 410**	$Fe(OH)_2$: 50	
	S_2O: 1.7		HCl: 370	PO_2: 15	
	H_2: 1.1		KOH: 260	**SO_3: 12**	
			COS: 190	**S_4: 12**	
			N_2: 160		
			NaF: 130		
BSE	**SO_2: 71**	CO_2: 0.56	**S_3: 930**	HCl: 65	
2000 K	**S_2: 18**	H_2: 0.32	Na: 520	NaF: 62	61.557
10 bar	H_2O: 3.9	**H_2S: 0.25**	NaOH: 460	**COS: 60**	
$\epsilon_s^{tot} = 4.77$	**SO: 3.1**	CO: 0.21	**S: 430**	K: 51	
Mass fraction [%]	**S_2O: 1.9**	**HS: 0.17**	KCl: 430	N_2: 48	
		NaCl: 0.12	HF: 210	OH: 36	
			KOH: 140	H: 29	
				KF: 25	
				PO_2: 18	
				$Fe(OH)_2$: 15	
				SO_3: 15	
				S_4: 14	

TABLE B3 (Continued)

Model	$n_{mol}/n_{tot} \geq 1\%$ [%]	≥ 0.1% [%]	≥ 100 ppm [ppm];	≥ 10 ppm [ppm];	mean molecular weight [amu]
BSE	O_2: 49	NaCl: 0.62	H_2: 800	CrO_3: 84	
2000 K	H_2O: 19	O: 0.47	HF: 760	$Fe(OH)_2$: 77	31.704
0.01 bar	Na: 12	NaF: 0.31	CO: 690	Fe: 71	
	SO_2: 6.3	KCl: 0.21	CrO_2: 520	Mn: 53	
	CO_2: 3.7	NaO: 0.13	H: 460	K^+: 30	
	NaOH: 3.2	KF: 0.13	FeO: 340	**SO_3: 26**	
	K: 1.1		NO: 170	HCl: 23	
	OH: 1.1		N_2: 150	PO: 23	
	PO_2: 1.1		**SO: 140**	MnO: 23	
	KOH: 1.0		KO: 130	SiO: 17	
				SiO_2: 14	
				TiO_2: 13	
BSE	H_2O: 47	NaOH: 0.50	HCl: 740	AlF_2O: 79	
2000 K	O_2: 28	OH: 0.49	NaF: 560	Cl: 56	31.252
1.0 bar	**SO_2: 13**	KCl: 0.44	Na: 430	**Na_2SO_4: 50**	
	CO_2: 8.0	HF: 0.21	**SO_3: 410**	K: 42	
	NaCl: 1.3	KOH: 0.16	N_2: 400	**SO: 39**	
			O: 350	NaO: 36	
			H_2: 260	H: 26	
			KF: 230	CrO_3: 18	
			NO: 210	PO_2: 15	
			CO: 200	HO_2: 14	
			$Fe(OH)_2$: 190	CrO_2: 14	
BSE	H_2O: 66	HCl: 0.80	N_2: 690	$(KCl)_2$: 95	
2000 K	**SO_2: 19**	KCl: 0.40	$(NaCl)_2$: 680	NaF: 86	30.724
100 bar	CO_2: 11	HF: 0.38	NaOH: 600	**Na_2SO_4: 70**	
	NaCl: 1.2	O_2: 0.28	**SO_3: 580**	$FeCl_2$: 58	
			OH: 580	**SO: 54**	
			H_2: 360	Cl: 51	
			CO: 280	KF: 35	
			$Fe(OH)_2$: 260	NO: 28	
			KOH: 190		
			AlF_2O: 180		
BSE	H_2O: 83	HCl: 0.58	N_2: 900	NaCl: 61	
1000 K	CO_2: 14	**H_2S: 0.56**		**COS: 21**	21.709
10 bar	H_2: 1.3	HF: 0.40		**SO_2: 11**	
		CO: 0.16			

TABLE B3 (Continued)

Model	$n_{mol}/n_{tot} \geq 1\%$ (%)	$\geq 0.1\%$ (%)	≥ 100 ppm (ppm);	≥ 10 ppm (ppm)	μ (amu)
BSE	O_2: 55	KCl: 0.54	CO: 700	**K_2SO_4: 98**	
2500 K	H_2O: 23	NaCl: 0.46	CrO_2: 660	$Mg(OH)_2$: 89	32.969
10 bar	**SO_2: 7.5**	Na: 0.42	H_2: 580	N_2: 83	
	CO_2: 4.4	KF: 0.36	$Fe(OH)_2$: 520	**Na_2SO_4: 81**	
	KOH: 2.8	O: 0.34	KO: 490	FeO: 78	
	NaOH: 2.7	NaF: 0.27	AlF_2O: 480	MnO: 40	
	OH: 1.6	HF: 0.22	NO: 400	Cl: 32	
		K: 0.17	**SO_3: 340**	$Ca(OH)_2$: 21	
		NaO: 0.12	PO_2: 330	K^+: 16	
			CrO_3: 300	Mn: 14	
			H: 190	Cl^-: 11	
			SO: 180		
			HCl: 140		
			HO_2: 130		
solar	H_2: 99.8		CO: 530	Mg: 75	
2000 K			H: 510	N_2: 66	2.0449
10 bar			H_2O: 380	SiO: 60	
				Fe: 37	
				H_2S: 21	

TABLE B4 Condensate families occurring in Figure 2.

Ca-Al-Ti	Silicates	Feldspar
$Ca_2MgSi_2O_7$[s] (akermanite)	SiO_2[l] (liquid quartz)	$KAlSi_3O_8$[s] (microcline)
Mg_2TiO_4[l] (liquid qandilit)	Mg_2SiO_4[l/S] (liquid and solid fosterite)	$CaAl_2Si_2O_8$[s] (anorthite)
$MgAl_2O_4$[l/s] (liquid and solid spinel)	$MgSiO_3$[l/s] (liquid and solid enstatite)	$NaAlSi_3O_8$[s] (albite)
$MgTi_2O_5$[l] (liquid Mg-dititanate)	Ca_2SiO_4[s] (larnite)	
$MnTiO_3$[s] (pyrophanite)	Fe_2SiO_4[s] (fayalite)	
Fe_2TiO_4[s] (ulvospinel)	Mn_2SiO_4[s] (tephroite)	
$FeAl_2O_2$[s] (hercynite)	$KAlSiO_4$[s] (kalsilite)	
$FeTiO_3$[s] (ilmenite)	$NaAlSiO_4$[s] (nepheline)	
$Mn_3Al_2Si_3O_{12}$[s] (spessartine)	$MnSiO_3$[s] (pyroxmangite)	
	Na_2SiO_3[l] (liquid NA-metasilicate)	
	$KAlSi_2O_6$[s] (leucite)	
	$CaMgSi_2O_6$[s] (diopside)	
Phyllosilicates	**Metal-oxides**	**Iron-oxides**
$KMg_3AlSi_3O_{12}H_2$[s] (phlogopite)	$MgFe_2O_4$[s] (magnesioferrite)	Fe_3O_4[s] (magnetite)
$NaMg_3AlSi_3O_{12}H_2$[s] (sodaphlogopite)	$MgCr_2O_4$[s] (picrochromite)	FeO[l/s] (liquid and solid ferropericlase)
	MnO[s] (manganosite)	
Sulphide	**P-compounds**	**Other**
FeS[s] (troilite)	$Ca_5P_3O_{13}H$[s] (hydroxyapatite)	NaCl[s] (halite)
	$Ca_5P_3O_{12}F$[s] (fluorapatite)	$KMg_3AlSi_3O_{10}F_2$[s] (fluorphlogopite)

The mass densities of these condensates have been co-added before plotting in Figure 2.

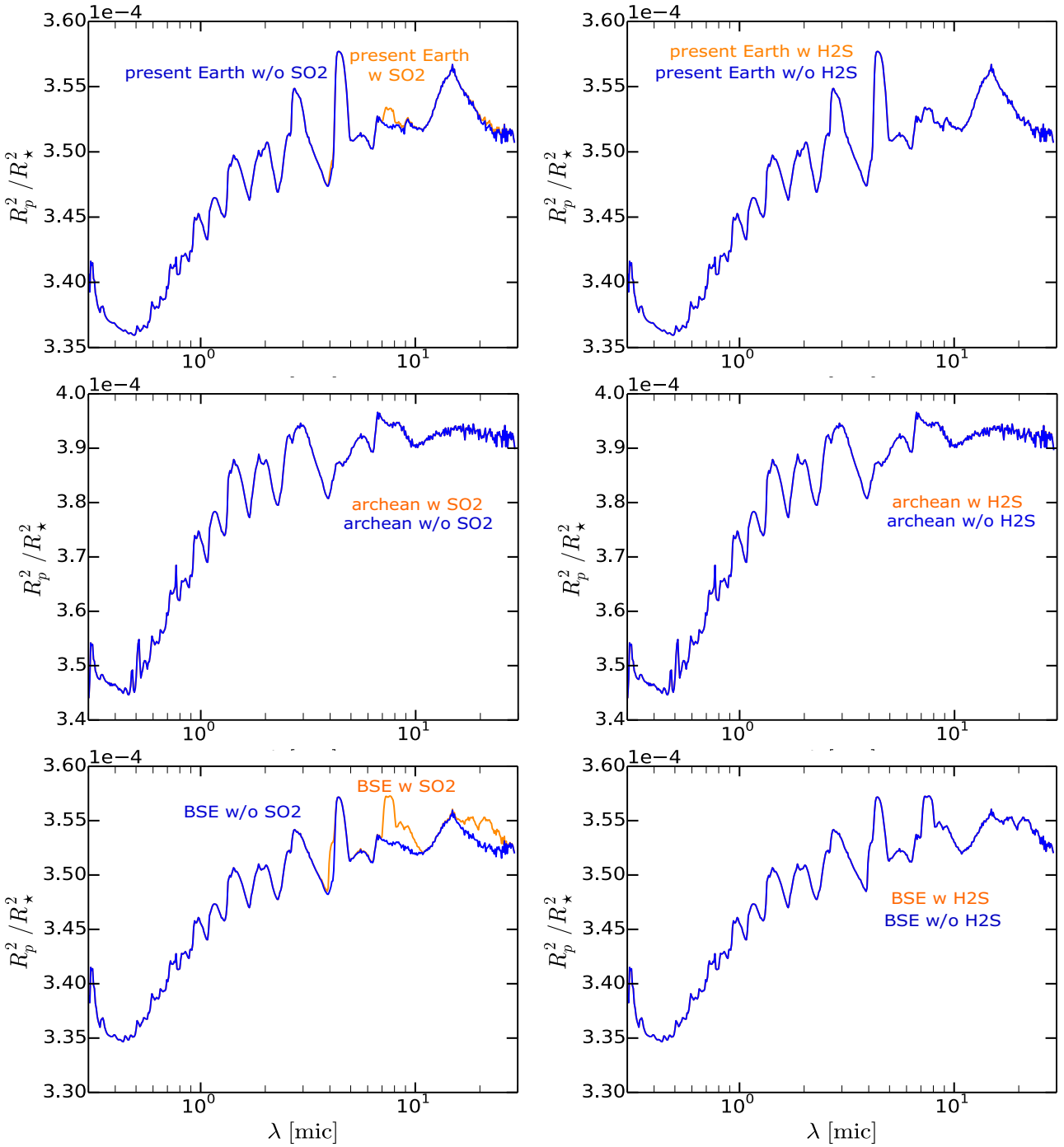

FIGURE C1 Impact of SO_2 and H_2S on the transmission spectra generated with ARCiS for isothermal atmospheres with $T = 2000$ K and $p_{surf} = 10$ bar. The model input parameters are listed in Table 3. On the left, the blue line shows the spectrum when the SO_2 line opacity is omitted. On the right, the blue line shows the spectrum when the H_2S line opacity is omitted.

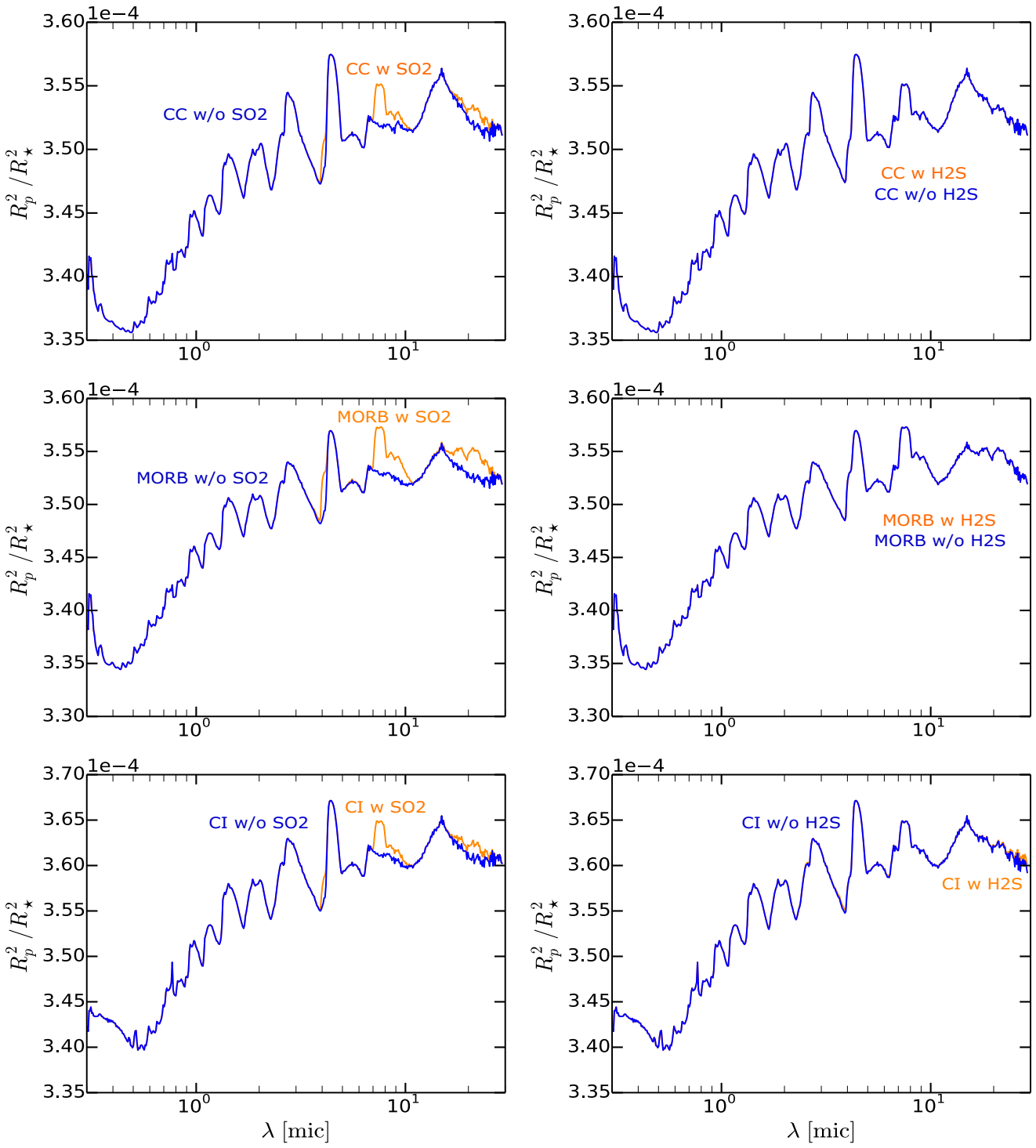

FIGURE C2 Same as Figure C1, but for different element compositions.

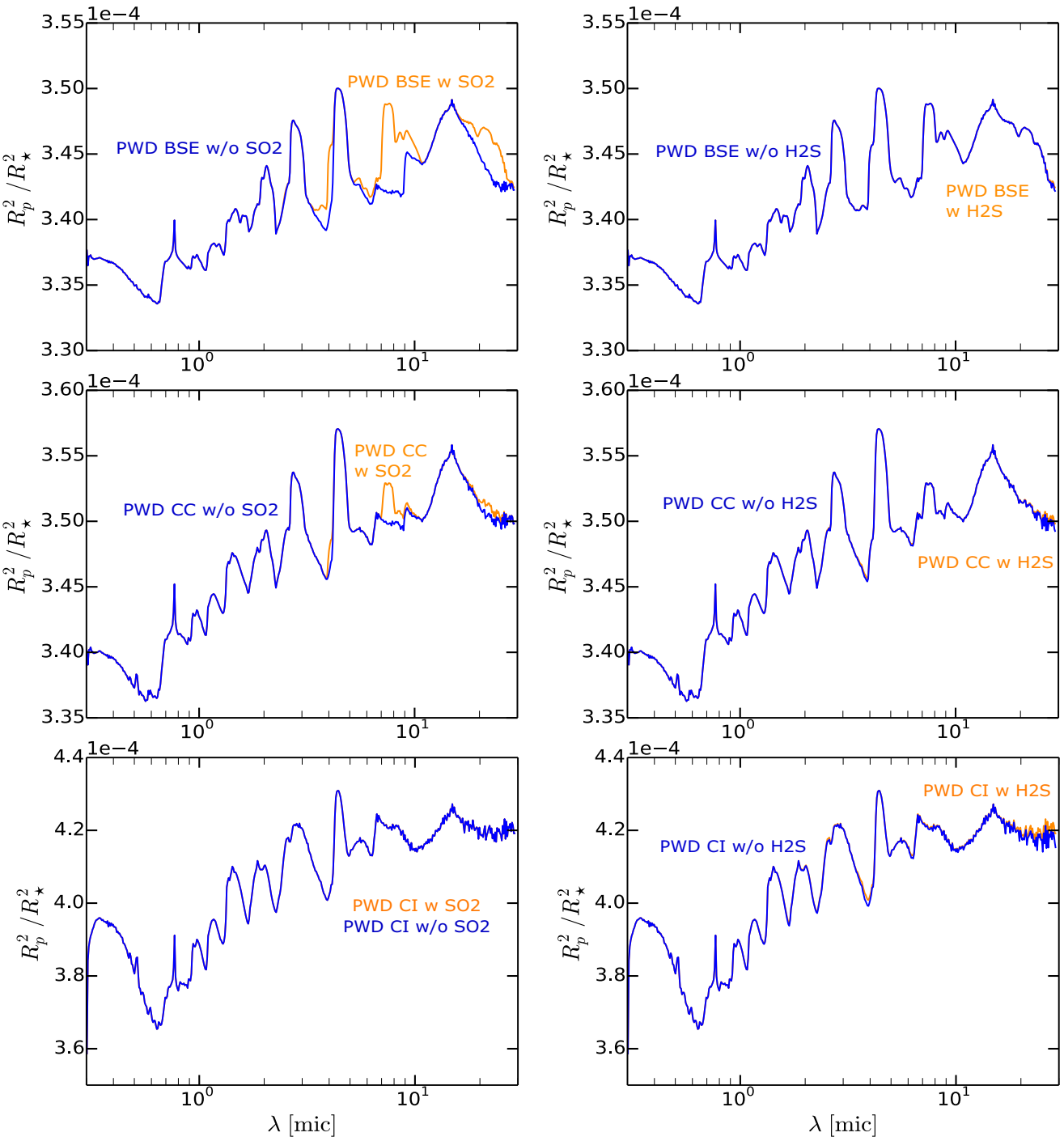

FIGURE C3 Same as Figure C1 but for element abundances derived from polluted white dwarfs.

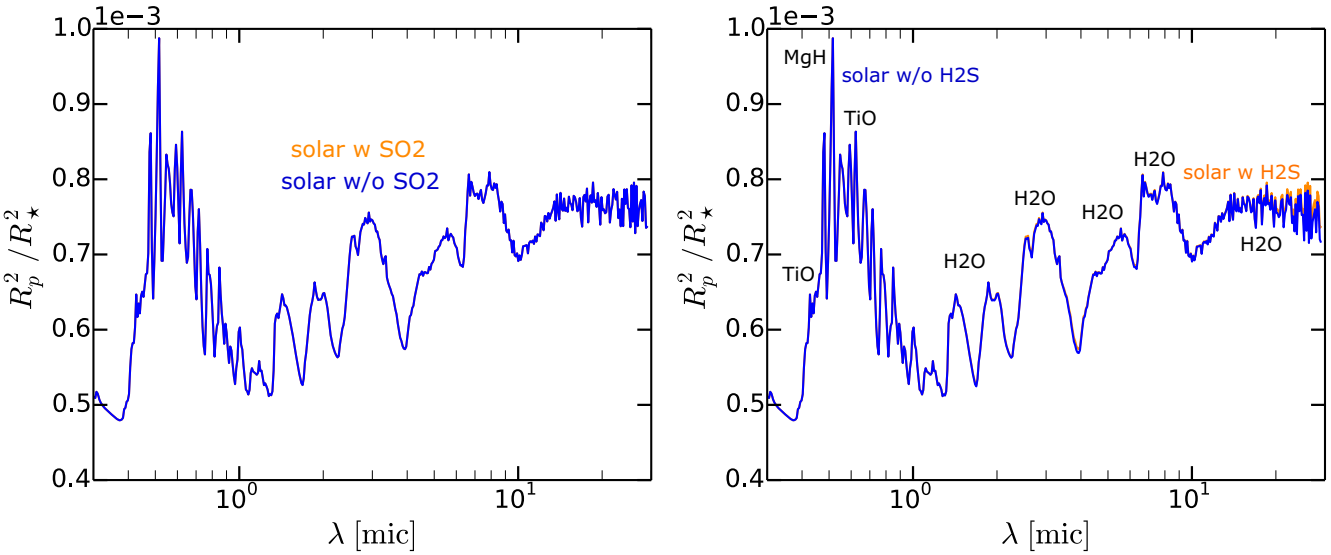

FIGURE C4 Same as Figure C1 but for solar element abundances, only showing the effect of SO_2, and H_2S. Both do not give rise to any strong spectral features. The towering absorption features at optical wavelengths are mainly due to TiO in between 0.38–1.03 μm with a sharp MgH feature between 0.47–0.61 μm.

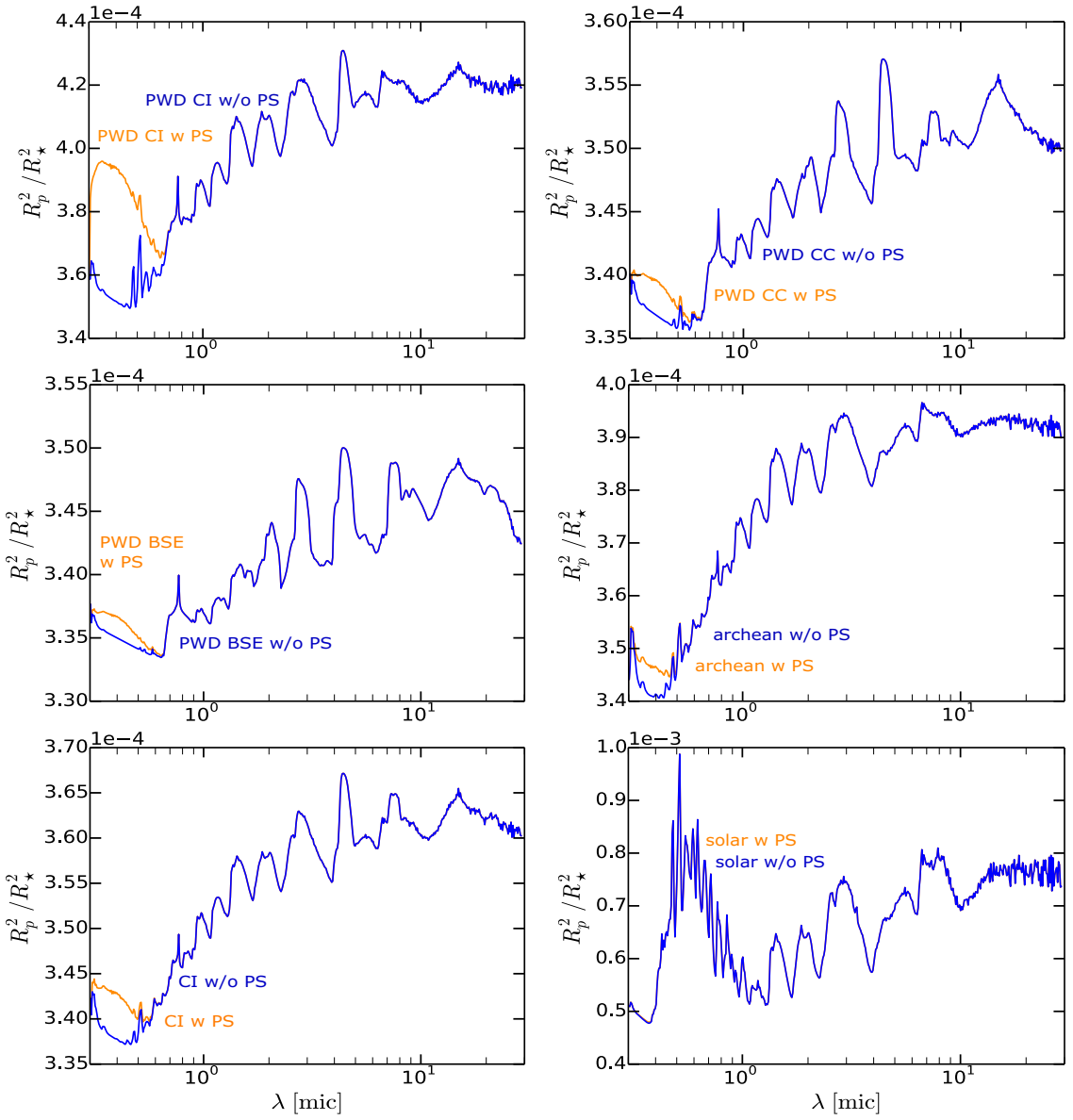

FIGURE C5 Transmission spectra obtained with ARCiS for Polluted White Dwarf element abundances, the Archean Earth, CI chondrite, and solar compositions at 2000 K and 10 bar. The orange curves show the complete results including PS, while the blue curves are the spectra obtained when the PS opacity has been set to zero. The ARCiS model parameter settings are listed in Table 3.

AUTHOR BIOGRAPHY

L. J. Janssen is a PhD student in Astronomy at Leiden Observatory. Their research is focusing on modelling atmospheres of warm, rocky exoplanets.